

Three-temperature radiation hydrodynamics with PLUTO

Tests and applications to protoplanetary disks

Dhruv Muley¹, Julio David Melon Fuksman¹, and Hubert Klahr¹

Max Planck Institut für Astronomie, Königstuhl 17, Heidelberg, DE 69117
e-mail: muley@mpia.de

Received 5 June 2023; accepted 3 August 2023

ABSTRACT

In circumstellar disks around T Tauri stars, visible and near-infrared stellar irradiation is intercepted by dust at the disk’s optical surface and reprocessed into thermal infrared; this subsequently undergoes radiative diffusion through the optically thick bulk of the disk. The gas component—overwhelmingly dominant by mass, but contributing little to the opacity—is heated primarily by gas-grain collisions. In hydrodynamical simulations, however, typical models for this heating process (local isothermality, β -cooling, two-temperature radiation hydrodynamics) incorporate simplifying assumptions that limit their ranges of validity. To build on these methods, we develop a “three-temperature” numerical scheme, which self-consistently models energy exchange between gas, dust, and radiation, as a part of the PLUTO radiation-hydrodynamics code. With a range of test problems in 0D, 1D, 2D, and 3D, we demonstrate the efficacy of our method, and make the case for its applicability to a wide range of problems in disk physics, including hydrodynamic instabilities and disk-planet interaction.

Key words. numerical methods — hydrodynamics — radiative transfer

1. Introduction

Protoplanetary disks—the rotationally-supported excess from the star-formation process—consist primarily of hydrogen and helium gas, with trace molecular species. Despite its preponderance by mass, this gas component has a low frequency-integrated opacity, making direct radiative heating and cooling inefficient. The disk’s energy exchange with the radiation field is instead mediated by the dust component, typically taken to constitute just 1% of its total mass. Chiang & Goldreich (1997) studied this process semi-analytically, finding that incident stellar radiation—which peaks in the visible and near-infrared for classical T Tauri stars—creates a superheated dust layer at a disk’s radial $\tau_r = 1$ surface. This layer reprocesses the radiation into the thermal infrared, half of which dissipates into interstellar space and half of which radiatively diffuses through dust grains in the optically thick disk midplane. The surrounding gas then thermally couples to the dust temperature structure via collisions. In turn, the density structure of the gas, and consequently that of the entrained dust that sets the $\tau_r = 1$ surface, adapt to maintain hydrostatic equilibrium.

By far, the most detailed models of protoplanetary disk thermal structure come from physical-chemical codes (e.g., Woitke et al. 2009; Bruderer et al. 2012; Bruderer 2013; Calahan et al. 2021), followed by standalone, multiwavelength radiative transfer codes (e.g., Dullemond et al. 2012; Whitney et al. 2013). However, the computational expense of these numerical algorithms, along with their implicit assumption that disks are static on timescales relevant to thermal physics, makes them intractable to include in dynamical problems. Hydrodynamical simulations must therefore use various parametrizations, of which the “locally isothermal” assumption—in which the temperature in each grid cell is fixed to its initial value—has been

historically important for its simplicity and ease of interpretation. But more recently, simulations of hydrodynamic instabilities and the anticyclonic vortices they generate (Malygin et al. 2017; Pierens & Lin 2018; Tarczay-Nehéz et al. 2020; Manger et al. 2021; Huang & Yu 2022), gaps and rings (Miranda & Rafikov 2019; Ziampras et al. 2020), spiral arms (Miranda & Rafikov 2020a,b), and circumplanetary disks (Fung et al. 2019) have revealed that the choice of disk thermodynamics prescription has a substantial influence on their morphology and behavior. The quality of disk observations continues to improve (e.g., Keppler et al. 2018; Ren et al. 2018; Teague et al. 2019; Pinte et al. 2022), and meaningfully interpreting them requires a more accurate, self-consistent treatment of disk heating and cooling in hydrodynamic models.

To this end, numerical radiation hydrodynamics (RHD) is promising. For computational efficiency, these simulations generally use the “grey approximation”, in which radiation energy densities, fluxes, and material opacities are averaged over frequency. One widely-used method in the study of protoplanetary disks (e.g., Klahr & Kley 2006; Kley et al. 2009; Bitsch et al. 2013; Flock et al. 2013; Binkert et al. 2023) is flux-limited diffusion (FLD; Levermore & Pomraning 1981), in which the radiative flux F_r is proportional to the gradient of radiation energy density E_r , subject to a limiter that ensures the system satisfies the speed-of-light limit, $|F_r| \leq cE_r$. Though FLD works well in optically thick regions, its definition of flux is limited in the thin limit, making it unable to produce anisotropic features in the radiation field such as beams or shadows. The M1 approximation (Levermore 1984) handles these issues with a separate evolution equation for flux. M1 can accurately reproduce both the optically thick diffusion and optically thin free-streaming limits, but has limitations in situations where free-streaming beams cross one another.

Differentiating between dust and gas temperatures is a comparatively recent development in RHD simulations. The star-formation simulations of Bate & Keto (2015), as well as the thermochemical disk simulations of Wang & Goodman (2017), Wang et al. (2019) and Hu et al. (2023), use equilibrium prescriptions to compute dust temperature. By contrast, Pavlyuchenkov & Zhilkin (2013), Pavlyuchenkov et al. (2015), and Vorobyov et al. (2020) use iterative Newton-Raphson schemes to self-consistently compute energy exchange between gas, dust, and radiation, while using FLD for radiation transport.

In what follows, we present our own three-temperature scheme, implemented within the PLUTO hydrodynamics code (Mignone et al. 2007). To compute energy exchange, we use Newton-Raphson iterations (albeit with differences from the aforementioned works), while to transport radiation, we use the M1 scheme already developed for PLUTO (Melon Fuksman & Mignone 2019; Melon Fuksman et al. 2021) to handle both the optically thick and thin regimes in protoplanetary disks. Section 2 describes our numerical method. Section 3 details our code tests: the first two (0D matter-radiation coupling and 1D Ensmann shock tube) have known reference solutions and demonstrate basic function, while the latter two (2D self-shadowing and 3D disk-planet interaction) illustrate applications to realistic disks. Section 4 provides a summation of our work and discusses possible future areas of research.

2. Method

2.1. Basic equations

We develop a strategy to solve the equations of radiation hydrodynamics, including a secondary dust fluid. In this work, we make the simplifying assumptions that dust grains are kinetically well-coupled to the gas (Stokes number $St \ll 1$) and that they have negligible inertia (globally constant dust-to-gas ratio $f_d \ll 1$)—in other words, both evolve with the same velocity field, and the dust has no momentum.

$$\frac{\partial \rho}{\partial t} + \nabla \cdot (\rho \mathbf{v}) = 0 \quad (1a)$$

$$\frac{\partial (\rho \mathbf{v})}{\partial t} + \nabla \cdot (\rho \mathbf{v} \mathbf{v}) = -\nabla p - \rho \nabla \Phi + \mathbf{S}_m + \mathbf{G} \quad (1b)$$

$$\frac{\partial E_g}{\partial t} + \nabla \cdot (E_g \mathbf{v}) = -\nabla \cdot ((p + \rho \Phi) \mathbf{v}) + S_m + X_{gd} + cG_g + S_g^{\text{irr}} \quad (1c)$$

$$\frac{\partial E_d}{\partial t} + \nabla \cdot (E_d \mathbf{v}) = -X_{gd} + cG_d + S_d^{\text{irr}} \quad (1d)$$

$$\frac{\partial E_r}{\partial t} + \hat{c} \nabla \cdot \mathbf{F}_r = -\hat{c}(G_g + G_d) \quad (1e)$$

$$\frac{\partial \mathbf{F}_r}{\partial t} + \hat{c} \nabla \cdot \mathbf{P}_r = -\hat{c} \mathbf{G} \quad (1f)$$

where ρ , \mathbf{v} , p represent the gas density, pressure, and velocity respectively. ρ_d is the dust density, while f_d is the dust-to-gas ratio, Φ is the gravitational potential, and $\{E_g, E_d, E_r\}$ are total energy densities for gas, dust, and radiation respectively. c is the speed of light, while the \hat{c} term is a “reduced speed of light” (Gnedin &

Abel 2001) which enables longer timesteps, but must nevertheless exceed all hydrodynamic velocities relevant to the problem (Skinner & Ostriker 2013).

We assume that the gas follows an ideal equation of state,

$$p = \rho_g k_B T_g / \mu m_H \quad (2)$$

where k_B is the Boltzmann constant, T_g the gas temperature, μ the mean molecular weight, and m_H the mass of a hydrogen atom. The adiabatic index $\gamma \equiv \partial \ln p / \partial \ln \rho$ is a constant, implying an *internal* (thermal) energy density

$$\xi_g = p / (\gamma - 1). \quad (3)$$

Because we do not consider the kinetic energy of dust in this work, the internal energy of dust, ξ_d , is equal to its total energy E_d . For consistency of notation in what follows, we additionally define a symbol $\xi_r \equiv E_r$.

Dust and gas exchange internal energy collisionally via the term

$$X_{gd} \equiv t_c^{-1} (r_{gd} \xi_d - \xi_g) \quad (4)$$

where t_c is the thermal relaxation time and $r_{gd} = k_B / \mu m_H f_d c_d (\gamma - 1)$ is the ratio of heat capacity per unit volume between gas and dust. c_d is the specific heat capacity of dust. We compute the gas cooling time t_c as a function of the dust-gas stopping time t_s , in the Epstein regime (Burke & Hollenbach 1983; Speedie et al. 2022)

$$t_c = \frac{2/3}{\gamma - 1} f_d^{-1} t_s \eta^{-1} \quad (5)$$

where η is an order-unity “accommodation coefficient” which we henceforth ignore. The corresponding dust cooling time is given by

$$t_{c,\text{dust}} = r_{gd}^{-1} t_c = \frac{2}{3} \frac{c_d}{k_B / \mu m_H} t_s. \quad (6)$$

In a realistic disk, the stopping time is computed by averaging over a grain-size distribution, which we describe as part of Section 3.3. The usual two-temperature radiation hydrodynamics represents the limit where $t_c \rightarrow 0$.

Net radiative heating/cooling is given for gas by

$$\begin{aligned} G_g \equiv & -\rho \kappa_g (a_r T_g^4 - \xi_r) \\ & - \rho (2\kappa_g - \chi_g) \boldsymbol{\beta} \cdot \mathbf{F}_r - \rho \chi_g \boldsymbol{\beta} \cdot (\xi_r \boldsymbol{\beta} + \boldsymbol{\beta} \cdot \mathbf{P}_r) \end{aligned} \quad (7a)$$

and likewise for dust by

$$\begin{aligned} G_d \equiv & -\rho \kappa_d f_d (a_r T_d^4 - \xi_r) \\ & - \rho f_d (2\kappa_d - \chi_d) \boldsymbol{\beta} \cdot \mathbf{F}_r - \rho f_d \chi_d \boldsymbol{\beta} \cdot (\xi_r \boldsymbol{\beta} + \boldsymbol{\beta} \cdot \mathbf{P}_r) \end{aligned} \quad (7b)$$

Similarly, the attenuation of radiative flux by gas is given by

$$\begin{aligned} \mathbf{G}_g \equiv & \rho \chi_g \mathbf{F}_r - \rho \kappa_g (a_r T_g^4 - \xi_r) \boldsymbol{\beta} \\ & - 2\rho \kappa_g (\boldsymbol{\beta} \cdot \mathbf{F}_r) \boldsymbol{\beta} - \rho \chi_g (\xi_r \boldsymbol{\beta} + \boldsymbol{\beta} \cdot \mathbf{P}_r) \end{aligned} \quad (7c)$$

and for dust by

$$\begin{aligned} \mathbf{G}_d \equiv & \rho f_d \chi_d \mathbf{F}_r - \rho f_d \kappa_d (a_r T_d^4 - \xi_r) \boldsymbol{\beta} \\ & - 2\rho f_d \kappa_d (\boldsymbol{\beta} \cdot \mathbf{F}_r) \boldsymbol{\beta} - \rho f_d \chi_d (\xi_r \boldsymbol{\beta} + \boldsymbol{\beta} \cdot \mathbf{P}_r) \end{aligned} \quad (7d)$$

involving absorption opacities κ , total (absorption plus scattering) opacities χ , temperatures T , the radiation constant $a_r =$

$4\sigma_{\text{SB}}/c$, and the radiation pressure tensor \mathbf{P}_r . Typically, κ is computed as a Planck average over frequency, while χ is computed as a Rosseland average. We define $\mathbf{G} \equiv \mathbf{G}_g + \mathbf{G}_d$; because our current implementation assumes dust follows the gas and has negligible inertia, it is this total \mathbf{G} that gets added to the gas momentum equation and integrated during the hydrodynamic step.

Each of the equations (7) can be divided into a β -independent and β -dependent part, $G = G^w + G'(\beta)$. The $G'(\beta)$ parts arise from a Lorentz transformation of the radiation-interaction terms from the fluid's comoving frame to the observer's frame, truncated in the mildly relativistic regime (Skinner & Ostriker 2013; Melon Fuksman & Mignone 2019). In protoplanetary disks, $\beta \ll 1$, so these terms are small and can be integrated explicitly.

The radiation pressure tensor $\mathbf{P}_r(E_r, \mathbf{F}_r)$ is evaluated according to the M1 closure (Levermore 1984), which accurately reproduces the free-streaming and diffusion limits:

$$\mathbf{P}_r^{ij} = D^{ij} E_r = E_r \left(\frac{1 - \Xi}{2} \delta^{ij} + \frac{3\Xi - 1}{2} n^i n^j \right) \quad (8)$$

in which

$$\Xi = \frac{3 + 4w^2}{5 + 2\sqrt{4 - 3w^2}} \quad (9)$$

where $\mathbf{n} = \mathbf{F}_r / \|\mathbf{F}_r\|$, $w = \|\mathbf{F}_r\|/E_r$, and δ^{ij} is the Kronecker delta.

S_d^{irr} and S_g^{irr} represent radiation emitted directly by the star, which has a higher-frequency spectrum than the dust-emitted radiation represented by E_r ; the source terms are computed (e.g., via ray tracing) at every hydrodynamic timestep, rather than being evolved dynamically as E_r and F_r are. S_m and S_m represent, respectively, energy and momentum source terms such as thermal conductivity and viscosity that are already implemented into PLUTO and integrated during the hydrodynamic step.

2.2. Conservation laws

With the reduced speed of light approximation, and ignoring non-ideal source terms other than $\mathbf{G}_g, \mathbf{G}_d, G_g, G_d, X_{gd}$, our system conserves the following modified total energy and momentum:

$$E_{\text{tot}} = E_r(c/\hat{c}) + E_g + E_d = \xi_r(c/\hat{c}) + \xi_g + \xi_d + \rho v^2/2 \quad (10)$$

$$\mathbf{P}_{\text{tot}} = \mathbf{F}_r/\hat{c} + \mathbf{p}_g \quad (11)$$

which reduce to the standard definitions when $c = \hat{c}$. As mentioned earlier, Skinner & Ostriker (2013) verified that this modification does not impact the dynamics of the system, provided that \hat{c} is much larger than hydrodynamic velocities characteristic of the system.

2.3. Operator splitting and timestepping

We solve the dusty radiation-hydrodynamic equations (1) using a Strang split, sandwiching a full step of the hydrodynamic terms Δt between two half-steps $\Delta t/2$ of the radiative terms. In quasi-conservative form:

$$\frac{\partial \mathcal{U}}{\partial t} + (\nabla \cdot \mathcal{F}_{\text{HD}} + \nabla \cdot \mathcal{F}_{\text{rad}}) = (\mathcal{S}_{\text{HD}} + \mathcal{S}_{\text{rad}}^{\text{imp}} + \mathcal{S}_{\text{rad}}^{\text{exp}}) \quad (12a)$$

¹ The Keplerian speed of an object orbiting a $1M_{\odot}$ at 0.01 au ($1R_{\odot}$ for a T Tauri star)—essentially the maximum attainable in a protoplanetary-disk context—is $\beta \approx 5 \times 10^{-3}$.

where \mathcal{U} is a vector of conserved variables, \mathcal{S} are source terms and \mathcal{F} are advective fluxes:

$$\mathcal{U} = (\rho, \rho v, E_g, E_d, E_r, \mathbf{F}_r)^{\top} \quad (12b)$$

$$\mathcal{F}_{\text{HD}} = (\rho v, \rho v v + p \mathbf{I}, (E_g + p + \rho \Phi) v, E_d v, 0, 0)^{\top} \quad (12c)$$

$$\mathcal{F}_{\text{rad}} = (0, 0, 0, 0, \hat{c} E_r, \hat{c} \mathbf{P}_r)^{\top} \quad (12d)$$

$$\mathcal{S}_{\text{HD}} = (0, -\rho \nabla \Phi + S_m, S_m, 0, 0, 0)^{\top} \quad (12e)$$

$$\mathcal{S}_{\text{rad}}^{\text{imp}} = (0, \mathbf{G}^w, X_{gd} + c G_g^w + S_g^{\text{irr}}, -X_{gd} + c G_d + S_d^{\text{irr}}, -\hat{c}(G_g + G_d), -\hat{c} \mathbf{G})^{\top} \quad (12f)$$

$$\mathcal{S}_{\text{rad}}^{\text{exp}} = (0, \mathbf{G}', c G'_g, c G'_d, -\hat{c}(G'_g + G'_d), -\hat{c} \mathbf{G}')^{\top} \quad (12g)$$

The overall timestep duration Δt is set by applying the Courant criterion to the hydrodynamical signal speeds v_{HD} . But because $\hat{c} \gg v_{\text{HD}}$, the radiation half-steps $\Delta t/2$ must be further divided into substeps of duration Δt_{rad} to ensure that the radiation subsystem meets its own Courant criterion. The integration of these substeps can take place through one of two implicit-explicit methods, IMEX1:

$$\begin{aligned} \mathcal{U}^{(1)} &= \mathcal{U}^n + \mathcal{R}_{\text{rad}}^n \Delta t_{\text{rad}} + \mathcal{S}_{\text{rad}}^{\text{imp}(1)} \Delta t_{\text{rad}} \\ \mathcal{U}^{(2)} &= \mathcal{U}^{(1)} + \mathcal{R}_{\text{rad}}^{(1)} \Delta t_{\text{rad}} + \mathcal{S}_{\text{rad}}^{\text{imp}(2)} \Delta t_{\text{rad}} \\ \mathcal{U}^{n+1} &= \frac{1}{2} (\mathcal{U}^{(1)} + \mathcal{U}^{(2)}) \end{aligned} \quad (13)$$

or IMEX-SSP(2,2,2), both analogous to second-order Runge-Kutta (Pareschi & Russo 2005):

$$\begin{aligned} \mathcal{U}^{(1)} &= \mathcal{U}^n + \mathcal{S}_{\text{rad}}^{\text{imp}(1)} a \Delta t_{\text{rad}} \\ \mathcal{U}^{(2)} &= \mathcal{U}^n + \mathcal{R}_{\text{rad}}^{\text{imp}(1)} \Delta t_{\text{rad}} \\ &\quad + \mathcal{S}_{\text{rad}}^{\text{imp}(1)} (1 - 2a) \Delta t_{\text{rad}} + \mathcal{S}_{\text{rad}}^{\text{imp}(2)} a \Delta t_{\text{rad}} \\ \mathcal{U}^{n+1} &= \mathcal{U}^n + \frac{\Delta t_{\text{rad}}}{2} (\mathcal{R}_{\text{rad}}^{(1)} + \mathcal{R}_{\text{rad}}^{(2)}) \\ &\quad + \frac{\Delta t_{\text{rad}}}{2} (\mathcal{S}_{\text{rad}}^{\text{imp}(1)} + \mathcal{S}_{\text{rad}}^{\text{imp}(2)}) \end{aligned} \quad (14)$$

where \mathcal{R}_{rad} is a shorthand for $-\nabla \cdot \mathcal{F}_{\text{rad}} + \mathcal{S}_{\text{exp}}^{\text{imp}}$ and $a = 1 - 1/\sqrt{2}$. \mathcal{R}_{rad} operators are integrated explicitly. However, the $\mathcal{S}_{\text{rad}}^{\text{imp}}$ operators, incorporating stiff terms such as opacity and gas-grain collision with characteristic timescales potentially much shorter than advective timescales, are integrated implicitly and are in general functions of t_{rad} .

In what follows, we concern ourselves with solving the implicit source terms. The explicit, advective radiative terms \mathcal{F}_{rad} , encompassing the transport of radiation energy density by radiative flux $\hat{c} \mathbf{F}_r$, and of radiative flux by the radiation pressure tensor $\hat{c} \mathbf{P}_r$, are updated using a Godunov scheme and Riemann solver as described in Melon Fuksman & Mignone (2019).

2.4. Momentum source terms

We update the radiative flux using the first-order implicit step

$$\mathbf{F}_r^{i+1} - \mathbf{F}_r^i = -\hat{c}\mathbf{G}^{i+1}\delta t = -\hat{c}\rho\delta t(\chi_d f_d + \chi_g)\mathbf{F}_r^{i+1} \quad (15)$$

where δt equals Δt_{rad} times the appropriate order-unity pre-factor for the implicit steps of equations 13 and 14. This can be solved analytically, by rearrangement. The resulting change in fluid momentum

$$(\rho\mathbf{v})^{i+1} - (\rho\mathbf{v})^i = -\hat{c}^{-1}(\mathbf{F}_r^{i+1} - \mathbf{F}_r^i)\delta t \quad (16)$$

can then be found straightforwardly by conservation.

From the final momenta, we can obtain the change in kinetic energy for gas

$$K_g^{i+1} - K_g^i = [(\mathbf{p}_g^{i+1})^2 - (\mathbf{p}_g^i)^2]/2\rho \quad (17a)$$

in which we make use of the fact that ρ is unchanged during a radiation timestep.

When the total dust and gas opacities χ are constant, the above equations must only be solved once. In general, however, they can be functions of temperature and density, and so must be solved before every iteration of the energy source terms. We describe these in the following section.

2.5. Energy source terms

The exchange of internal energies ξ between dust, gas, and radiation, is updated as follows:

$$\begin{aligned} \xi_d^{i+1} - \xi_d^i &= -(t_c^{-1})^{i+1} [r_{gd}\xi_d^{i+1} - \xi_g^{i+1}] \delta t \\ &\quad - (t_d^{i+1})^{-1} [a_r(T_d^{i+1})^4 - \xi_r^{i+1}] \delta t \end{aligned} \quad (18a)$$

$$\begin{aligned} \xi_g^{i+1} - \xi_g^i &= + (t_c^{-1})^{i+1} [r_{gd}\xi_d^{i+1} - \xi_g^{i+1}] \delta t \\ &\quad - (t_g^{i+1})^{-1} [a_r(T_g^{i+1})^4 - \xi_r^{i+1}] \delta t \end{aligned} \quad (18b)$$

with the dust temperature $T_d = \xi_g/(\rho c_d f_d)$ and the gas temperature $T_g = \xi_g/(\rho k_B/\mu)$. To simplify notation, we have introduced the symbols $t_d = (c\rho\kappa_d f_d)$ (the timescale required for light to travel one mean free path through dust) and $t_g = (c\rho\kappa_g)^{-1}$ (the same, for gas); the relevant absorption opacities κ and cooling times t_c are in general functions of temperature and density. δt indicates the length of an implicit partial step, which is Δt_{rad} in the case of IMEX1, (13) and $a\Delta t_{\text{rad}}$ or $(1 - 2a)\Delta t_{\text{rad}}$, depending on the specific partial step, in the case of IMEX-SSP(2,2,2) (14).

The i superscripts indicate quantities at the beginning of the implicit partial step, while those with $i + 1$ indicate those at the end. ξ_r^{i+1} is not computed directly in the above system, but is given by conservation of energy, modified to account for the reduced speed of light and the irradiation source terms S_g^{irr} and S_d^{irr} :

$$\begin{aligned} \xi_r^{i+1} - \xi_r^i &= -(\hat{c}/c) [(\xi_d^{i+1} - \xi_d^i) + (\xi_g^{i+1} - \xi_g^i)] \\ &\quad + (\hat{c}/c)(S_g^{\text{irr}} + S_d^{\text{irr}})\delta t \end{aligned} \quad (18c)$$

We insert ξ_r^{i+1} from equation 18c into equations eqs. (18a) and (18b) and solve the system using a multidimensional Newton's method (detailed in Appendix A). All equations operate on cell-averaged quantities. We note that the values of the stellar irradiation source term S_d^{irr} are updated, by ray-tracing, only at the

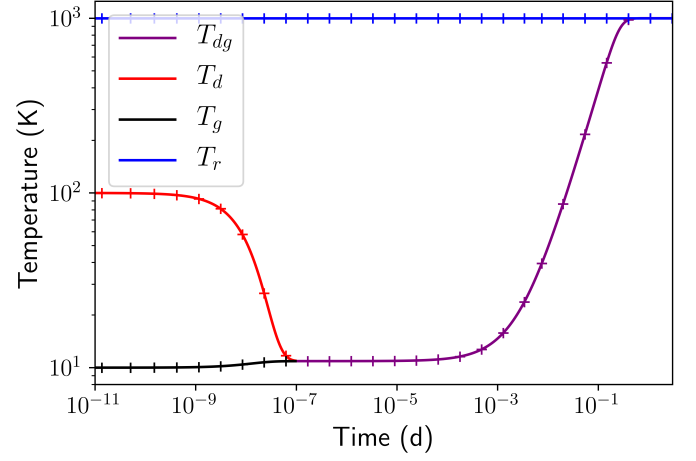


Fig. 1. A 0D test of our three-temperature scheme, for which we set the dust-gas stopping time $t_s = 10^{-9}t_0 = 8 \times 10^{-9}$ d and the opacity $\kappa_d = 3.9 \text{ cm}^2 \text{ g}^{-1}$. Pluses indicate numerical results, while solid lines indicate analytical solutions taken from equations 21 (red, black) and 24 (purple). Because the system is dominated by radiation energy, the radiation temperature (blue) is nearly constant throughout the system's evolution.

start of each overall timestep Δt , even though their contribution to the energy density is added during each radiation substep. For the tests presented here, we set $S_g^{\text{irr}} = 0$, but we foresee it being useful in the future to model photoelectric or line heating in the upper disk (Dullemond et al. 2007).

Our implementation has the advantage of conserving total modified energy to machine precision, and converging within a small number of iterations (typically $\lesssim 5 - 10$ in disk-planet interaction simulations, even with temperature- and density-dependent cooling times). Moreover, it accommodates temperature change that is rapid compared to Δt_{rad} , making it useful in nonequilibrium cases such as accretion shocks, subject to constraints set by the reduced speed of light approximation.

3. Tests

To verify the accuracy of our scheme and demonstrate its applicability to protoplanetary disks, we run test problems in 0D, 1D, 2D, and 3D. For the tests we present, we use third-order Runge-Kutta (RK3) timestepping with third-order weighted essentially non-oscillatory (WENO3) reconstruction (Yamaleev & Carpenter 2009) and a Harten-Lax-van Leer-Contact (HLLC) Riemann solver for both the gas and radiation. The sole exception is our 2D disk self-shadowing test, in which large contrasts in temperature, density, and velocity emerge in high, close-in regions of the disk. As such, for this problem, we opt for second-order Runge-Kutta (RK2) time integration and piecewise linear method (PLM) spatial reconstruction with a van Leer flux limiter.

3.1. 0D test: radiation-matter coupling

For our first set of tests, we consider a zero-dimensional setup probing only the local evolution of gas, dust, and radiation temperatures. We turn off the hydrodynamic equations and radiation advective terms, and set irradiation source terms and radiative flux to zero, in order to isolate the effects of radiation-matter coupling. In this case, we can write the evolution of internal en-

ergies concisely in terms of $\xi = (\xi_d, \xi_g)^\top$:

$$\frac{\partial \xi}{\partial t} = [\mathbf{C}\xi] + [\mathbf{A}_{\text{tot}} + \mathbf{A}\xi + \mathbf{Q}(\xi)] \quad (19)$$

where \mathbf{A} includes linear absorption terms, \mathbf{C} the collisional terms, \mathbf{A}_{tot} the constant absorption terms, and \mathbf{Q} the nonlinear emission terms:

$$\mathbf{C} = \begin{bmatrix} -t_c^{-1} r_{gd} & +t_c^{-1} \\ +t_c^{-1} r_{gd} & -t_c^{-1} \end{bmatrix} \quad (20a)$$

$$\mathbf{A} = \frac{\hat{c}}{c} \begin{bmatrix} -t_d^{-1} & -t_d^{-1} \\ -t_g^{-1} & -t_g^{-1} \end{bmatrix} \quad (20b)$$

$$\mathbf{A}_{\text{tot}} = \xi_{\text{tot}} \hat{c} / c \left(t_d^{-1}, t_g^{-1} \right)^\top \quad (20c)$$

$$\mathbf{Q}(\xi) = -a_r \left(t_d^{-1} T_d^4, t_g^{-1} T_g^4 \right)^\top \quad (20d)$$

For our setup, we use a gas density of $\rho_g = 7.78 \times 10^{-18} \text{ g cm}^{-3}$ with a dust-to-gas ratio $f_d = 10^{-2}$ and stopping time $t_s = 10^{-9} t_0$, where $t_0 = 8$ days is the code unit for time. We use a fixed opacity $\kappa_d = 3.9 \text{ cm}^2 \text{ g}^{-1}$ and $\hat{c} = c$. At $t = 0$ we set $T_g = 10^1 \text{ K}$, $T_g = 10^2 \text{ K}$, and $T_r = 10^3 \text{ K}$. The specific heat capacity of the gas c_g is defined by its mean molecular weight $\mu = 1$ and adiabatic index $\gamma = 7/5$; we set the dust specific heat capacity c_d equal to that of the gas. By analogy with the determination of Stokes number $\text{St} \equiv t_s \Omega$ of quasi-Keplerian disks, we can compute a characteristic timescale for this system, $t_{\text{cross}} = l_{\text{cross}} / v_{\text{cross}}$, where l_{cross} and v_{cross} are the length and velocity scales of interest. In this case, we choose a $l_{\text{cross}} = (\kappa_d f_d \rho_g)^{-1} = 3.38 \times 10^{18} \text{ cm}$ —the mean free path of the system—and a $v_{\text{cross}} = (k_B T_g / \mu m_p)^{1/2} = 287 \text{ m s}^{-1}$. This yields a $t_{\text{cross}} = 3.6 \times 10^6 \text{ y}$, or a $t_s / t_{\text{cross}} = 5.87 \times 10^{-18}$.

The system should relax to an equilibrium state in which dust, gas, and radiation have equivalent effective temperatures—specifically, $\xi_d = \xi_g / r_{gd} = c_g \rho_g (\xi_r / a_r)^{1/4}$. Furthermore, in several special cases, it has analytical solutions against which our numerical scheme can be tested. For instance, when collisional energy exchange between gas and dust happens much faster than absorption, the system has a solution in terms of matrix exponentials:

$$\xi(t) \approx \exp[\mathbf{C}t] \xi_0 \quad (21)$$

Given our simulation parameters, we find that equation 21 is a good description of the temperature evolution at early times. We plot its predictions for T_g and T_d as black and red lines respectively in 1. On timescales $t > t_c / (1 + r_{gd}) \approx t_s$, such a system reaches a quasi-steady state where $\xi_d = \xi_g / r_{gd}$ —in other words, the temperatures of dust and gas become equal.

By contrast, when the absorption and emission terms dominate over collisions, and additionally the system is radiation-energy dominated throughout its evolution (i.e., $(c/\hat{c})\xi_r \equiv (\xi_{\text{tot}} - \xi_d - \xi_g) \gg \xi_g + \xi_d$), \hat{c} drops out of the equations and we get:

$$\frac{\partial}{\partial t} \begin{bmatrix} \xi_d \\ \xi_g \end{bmatrix} \approx \begin{bmatrix} t_d^{-1} (\xi_{r,0} - a_r (\xi_d / \rho_d f_d c_d)^4) \\ t_g^{-1} (\xi_{r,0} - a_r (\xi_g / \rho_g c_g)^4) \end{bmatrix} \quad (22)$$

Each element of 22 is identical to the form found in eq. (69) and Figure 5 of Melon Fuksman & Mignone (2019), and yields an implicit analytic relation that can be inverted by root-finding:

$$2Mt = \text{Re}(\arctan(\omega) + \text{arctanh}(\omega)) - \text{Re}(\arctan(\omega_0) + \text{arctanh}(\omega_0)) \quad (23)$$

where $M_d = (a_r / \xi_{r,0})^{1/4} \xi_{r,0} t_d^{-1} / (\rho_d f_d c_d)$, $\omega_d = (a_r / \xi_{r,0})^{1/4} (\xi_d / f_d \rho_d c_d)$, and $\omega_{d,0} = \omega_d(t = 0)$; M_g and ω_g are obtained likewise. ξ_r is assumed constant throughout the evolution of the system.

When the collision timescale is much shorter than the absorption-emission timescale, but the dust and gas are already in collisional equilibrium, we can obtain yet another special case by summing the two rows of eq. (22):

$$\frac{\partial \xi_d}{\partial t} = \frac{t_d^{-1} + t_g^{-1}}{1 + r_{gd}} (\xi_{r,0} - a_r (\xi_d / \rho_d f_d c_d)^4) \quad (24)$$

where we constrain $\xi_d = \xi_g / r_{gd}$. The solution to equation (24) is also in the form of (23), with $M_{dg} = (a_r / \xi_{r,0})^{1/4} \xi_{r,0} (t_d^{-1} + t_g^{-1}) ((1 + r_{gd}) \rho_d f_d c_d)^{-1}$ and $\omega_{dg} = (a_r / \xi_{r,0})^{1/4} (\xi_d / \rho_d f_d c_d)$.

We plot equation (24) as a purple curve in Figure 1. Our scheme accurately handles the regime where dust and gas temperatures are well-coupled, showing that it is effective at reproducing the “two-temperature” limit of typical radiation-hydrodynamics simulations.

3.2. 1D test: Subcritical dusty radiative shock

Having verified that our scheme accurately reproduces three-temperature static thermal coupling, we seek to study its performance in a dynamical setting. To this end, we run a modified version of the 1D subcritical radiative shock in Ensmann (1994), a standard test for radiation-hydrodynamic codes (see e.g., section 4.1 of Melon Fuksman et al. 2021, and references therein) incorporating sharp transitions in temperature and opacity.

In this setup, our domain spans the interval $[0, 7 \times 10^{10} \text{ cm}]$. The initial gas density is $\rho_g = 7.78 \times 10^{-10} \text{ g cm}^{-3}$, with a dust-to-gas ratio $f_d = 10^{-2}$. Dust, gas, and radiation temperatures are all initialized in equilibrium, $T_r = T_g = T_d = 10 \text{ K}$; $\gamma = 7/5$, $\mu = 1$, and $c_d = c_g$ are the same as in the 0D case. The dust absorption opacity is set such that the inverse mean free path of radiation through dust, $l_d^{-1} \equiv \kappa_d \rho_d = 3.1 \times 10^{-10} \text{ cm}^{-1}$, with dust scattering opacity $\chi_d - \kappa_d$, and gas total opacity χ_g , both assumed to be zero. To form the shock, given our otherwise equilibrium initial conditions, we set an initial gas velocity $v_x = -6 \text{ km s}^{-1}$, and impose a reflective condition on the left boundary. We fiducially choose a reduced speed of light $\hat{c} = 10^{-3} c$ and a spatial resolution $N_x = 1200$ cells; these figures give results consistent with those of our tests (not shown) at $\hat{c} = c$, and both higher and lower resolutions.

We test stopping times $t_s = \{10^{-7}, 10^{-4}, 10^{-1}\} t_0$, where we again use $t_0 = 8 \text{ d}$ as the code unit for time. For this problem, we define the characteristic timescale using l_d as our length scale and v_x as the velocity scale, yielding a $t_{\text{cross}} = 7.78 \times 10^{-2} t_0$ and $t_s / t_{\text{cross}} = 1.28 \times \{10^{-5}, 10^{-2}, 10^1\}$. The last case is included to demonstrate the properties of our code when dust and gas have weak *thermal* coupling, although the long t_s / t_{cross} would also allow for relative motion between dust and gas, which we do not model.

In Figure 2, we plot temperature snapshots at $t = 0.054 t_0 = 3.75 \times 10^4 \text{ sec}$ for all stopping times, selecting $N_x = 1200$ as our fiducial resolution. For $t_s = 10^{-1}$, the gas temperature is that of a standard hydrodynamic shock. In the pre-shock region dust and gas are essentially in equilibrium; in the post-shock region, by contrast, the dust heats at a rate $T_{d,\text{coll}} \approx (T_g - T_d) t_{c,\text{dust}}^{-1} \approx (T_{g,+} - T_{d,-}) t_{c,\text{dust}}^{-1}$, where minuses and pluses denote pre- and post-shock quantities respectively. Deeper in the post-shock region, this trend breaks down, as radiative cooling (which scales

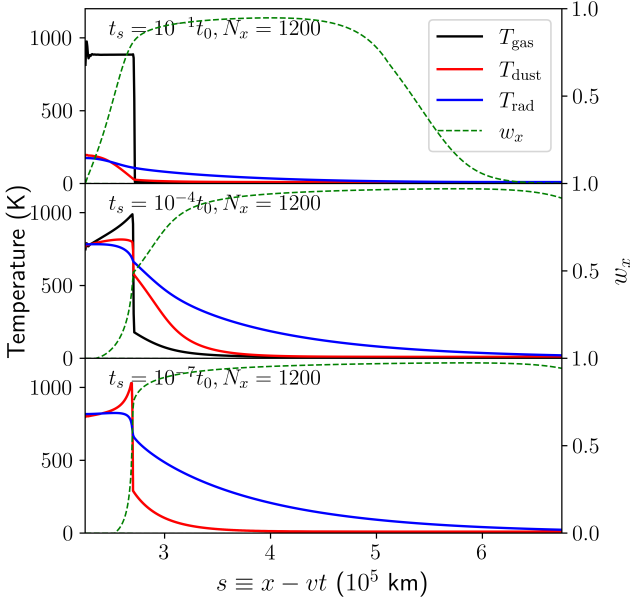


Fig. 2. Temperature profiles in the dusty radiative shock test at $t = 0.054t_0 = 3.75 \times 10^4$ sec, for a variety of stopping times. For $t_s = 10^{-1}$, the gas temperature is that of a standard hydrodynamic shock, with only weak losses to dust and radiation; for $t_s = 10^{-7}$, T_d and T_g have come into equilibrium, and they (along with w_x and T_r) match the results of the two-temperature radiative shock tests in section 4.1 of (Melon Fuksman et al. 2021) (note that the signed “reduced flux” $w_x \equiv F_x/E_r$ is denoted as f in their work).

as $\dot{T}_{d,\text{rad}} \approx -cI_d^{-1}a_r(T_{d,-}^4 - T_{r,-}^4)/c_d\rho_d$ becomes sufficient to counteract the effects of collisional heating.

In the $t_s = 10^{-4}t_0$ case, the cooling time $t_{c,\text{dust}}$ is short, and T_d increases rapidly immediately after encountering the shock. Because the collisional heating rate is faster than for $t_s = 10^{-1}t_0$, the radiative cooling rate, and thus the maximum post-shock dust temperature, must be correspondingly higher. In the pre-shock region, this process is inverted: radiation propagating from the shock front heats the dust above its initial preshock value, and via collisions, the gas. For the strongly coupled case, with $t_s = 10^{-7}t_0$, dust and gas are in collisional equilibrium, and we recover the two-temperature results of Melon Fuksman et al. (2021). Because the Courant-limited radiation timestep $\Delta t_{\text{rad}} \approx \Delta x/\hat{c}$ is much longer than our dust coupling time, this result demonstrates the efficacy of our IMEX scheme in the stiff regime.

In these 1D simulations, changes in the radiation field are driven by collisional heating of the dust, and ultimately by the rightward motion of the shock front—a process much slower than radiation propagation or absorption/emission. In this regime, we can drop the time derivative terms in Equation 1f and take the nonrelativistic limit

$$\nabla(\Xi E_r) \approx -\rho_d \kappa_d F_x = -I_d^{-1} F_x \quad (25)$$

where the Ξ parameter is defined in Equation 9 as a function of the “reduced flux” w . Adding a sign to this reduced flux $w_x = F_x/E_r = \pm w$ and rearranging terms, we get that

$$\partial_{w_x}(\Xi)\nabla(w_x) \approx -(I_d^{-1}w_x + I_r^{-1}\Xi) \quad (26)$$

where $I_r^{-1} \equiv \nabla(E_r)E_r^{-1}$ is the relative rate of change in the radiation field. In other words, variations in the radiation field on length scales shorter (longer) than some critical scale $l_d|\Xi|w_x|^{-1}$ drive (damp) the flux.

This is clearly visible in Figure 2: in the $t_s = 10^{-1}t_0$ case, the relatively moderate gradient in radiation energy means that the transition from the $w_x \approx 0$ diffusion regime to the $w_x \approx 1$ free-streaming regime occurs smoothly over the post-shocked region. For $s \gtrsim 5 \times 10^5$ km, radiation from the shock front is sufficiently extinguished that the radiation field is dominated by the flat 10 K background; accordingly, $|I_r| \rightarrow \infty$ and w_x damps to zero.

By contrast, the $t_s = 10^{-7}t_0$ case has a flat radiation field for much of the post-shock region, but a sharper one in the immediate vicinity of the shock, creating an abrupt transition between the diffusion and free-streaming regimes. Because the post-shock radiation field is stronger in this case, it propagates to a greater optical depth before decaying into the flat $T_r = 10$ K background, so the w_x damping seen in the $t_s = 10^{-1}t_0$ simulation is not visible in the plotted region. The $t_s = 10^{-4}t_0$ case represents an intermediate case between these two extremes.

3.3. 2D test: self-shadowing instability

The self-shadowing or thermal wave instability (SSI; see e.g., D’Alessio et al. 1999; Dullemond 2000; Watanabe & Lin 2008; Flock et al. 2020; Wu & Lithwick 2021) has been proposed as a planet-free means of generating gaps and rings in circumstellar disks. SSI begins with a disk in initial radiative and (vertical) hydrostatic equilibrium. A small perturbation to the disk’s radial $\tau_r = 1$ surface would create slightly raised regions which absorb more stellar irradiation, and lowered, obscured regions which absorb less. To maintain hydrostatic equilibrium, the raised regions would increase in scale height (and thus absorb even more starlight), while the lowered ones would decrease in scale height and absorb even less.

SSI is readily reproduced in 1+1D simulations that parametrize the vertical extent of a disk (e.g., Ueda et al. 2021). It can also be generated (e.g., Ueda et al. 2019) by an iterative procedure that first uses radiative transfer to obtain a disk’s temperature profile, given its density structure; assuming hydrostatic equilibrium, this profile is then used to recompute the density structure for the next iteration.

However, Melon Fuksman & Klahr (2022) find that this picture breaks down with additional physics: in their two-temperature radiation hydrodynamics simulations, SSI bumps do not grow from noise, and decay rapidly even when artificially introduced via the aforementioned iterative procedure. They explain their results by arguing that the erosion of perturbations at the $\tau_r = 1$ surface—caused by in-plane radiation transport and the hydrostatic adaptation of the gas in the upper disk—occurs on timescales much faster than the classical vertical radiative heating timescale of the disk (Hubeny 1990; Zhu et al. 2015; Zhang & Zhu 2020)

$$t_{\text{SSI,rad}} = \frac{3(\tau_v + \tau_v^{-1})(\Sigma_d c_d + \Sigma_g c_g)}{4ca_r(T_{\text{irr}}^2 + T_{\text{d,mid}}^2)(T_{\text{irr}} + T_{\text{d,mid}})} \quad (27)$$

where $\tau_v = \kappa_d(\Sigma_d/2)$ is the vertical optical depth of the disk to the midplane in thermal infrared, Σ_d and Σ_g are the dust and gas surface densities, T_{irr} is the equilibrium temperature of the stellar irradiation field in the optically thin region of the disk, and $T_{\text{d,mid}}$ is the dust midplane temperature. Physically, this means that bumps at the optical surface decay long before they can impact the temperature at the disk surface.

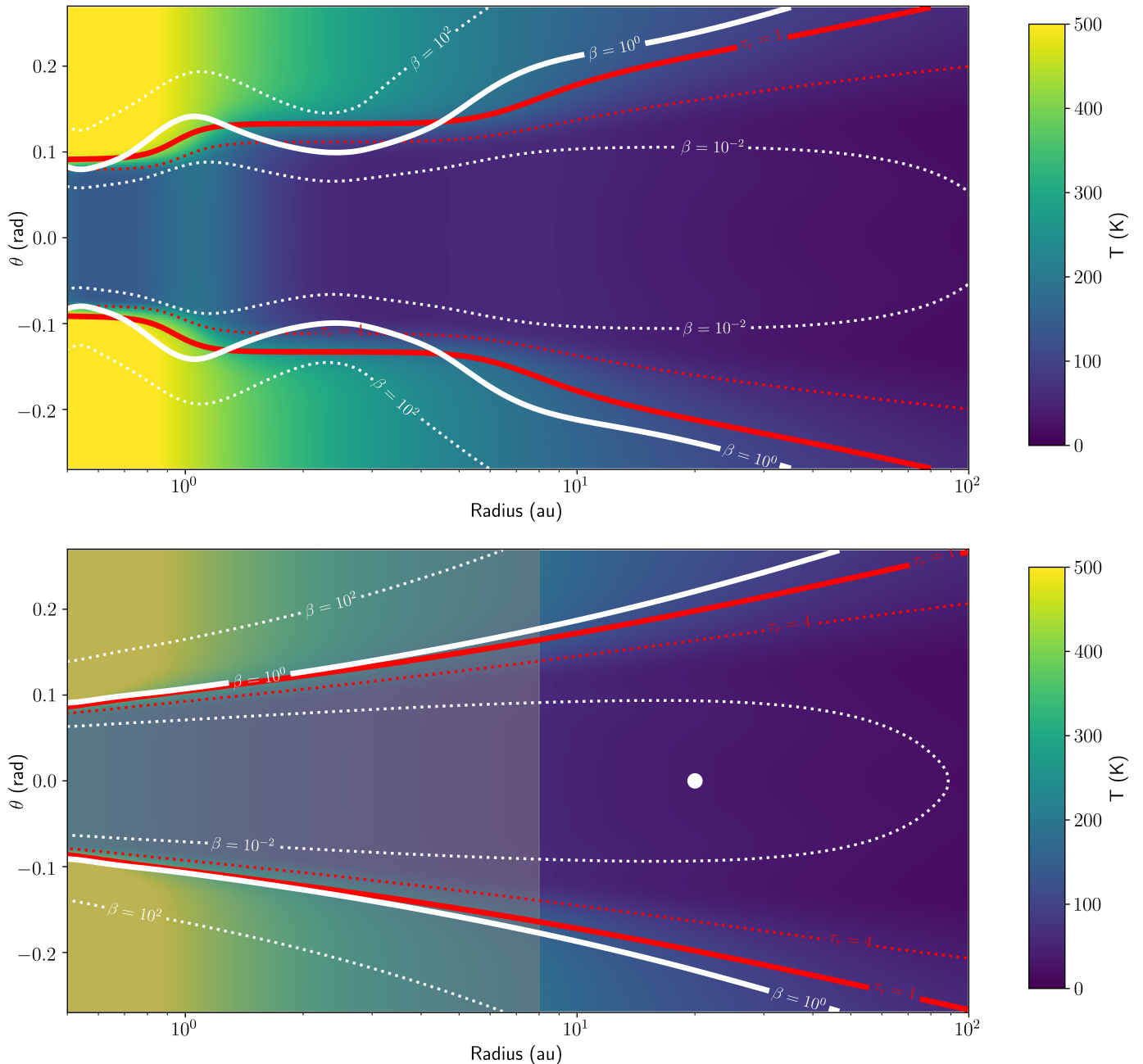


Fig. 3. *Above*, initial $T_d = T_g$ for our 2D self-shadowing test (3.3), based on dg3t100 from (Melon Fuksman & Klahr 2022); *below*, the same for our 3D planet-driven spiral test (3.4), based on dg3t0.1. We overplot contours for radial optical depth τ_r (red) (computed using opacities Planck-averaged over the stellar spectrum) and cooling parameter $\beta \equiv t_c \Omega$. Our calculations of these quantities assume an MRN distribution of small silicon-graphite grains, and a $1M_\odot$ classical T Tauri star as the source of light and gravity. In the lower plot, a white dot indicates the position of the embedded $1M_J$ planet, while grey shading covers the region outside the $r = [8, 100]$ au boundaries of our 3D simulation.

A nonzero coupling time between gas and dust temperatures would allow a temperature perturbation at the $\tau_r = 1$ surface to establish itself in the underlying disk column by propagating only through the dust—a much faster process than that implied by equation (27), in which the gas and dust are heated together. The subsequent adaptation of the gas’s vertical structure to this already-established background would conform better to the assumptions of iterative methods which have been successful in reproducing the SSI. Moreover, such a coupling time would delay the response of the perturbed $\tau_r = 1$ gas to in-plane radiation transport, limiting the radial diffusion of SSI bumps. **We emphasize that nothing about this prediction accounts for the**

effects of nonzero coupling times between dust and gas velocities on the evolution of the SSI, a topic which we defer to future work.

In the context of protoplanetary disks, a realistic coupling time may be found by computing t_s with the Epstein drag law (see e.g., Speedie et al. 2022; Melon Fuksman et al. 2023)

$$t_s = \frac{\rho_{\text{dg}} \langle a_{\text{dg}}^3 \rangle}{\rho_g v_{\text{th}} \langle a_{\text{dg}}^2 \rangle} \quad (28)$$

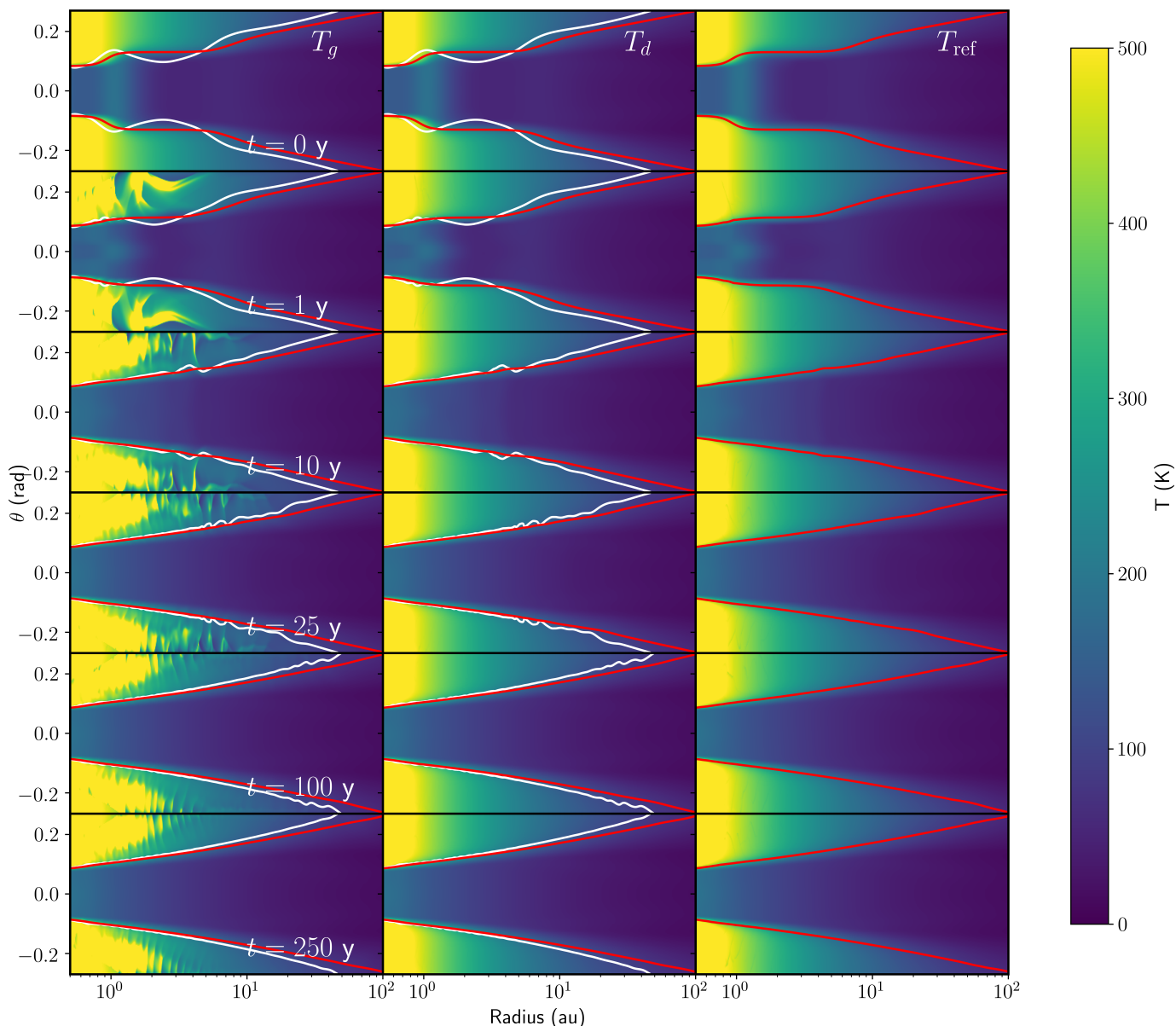


Fig. 4. Two-dimensional temperature profiles from our SSI tests. The T_g (left) and T_d (middle) columns come from our simulations with realistic t_s , whereas T_{ref} (right) is from our reference simulations with $t_s = (2\pi)^{-1} \times 10^{-10}$ y. For ease of interpretation, we overplot $\beta = 1$ (white) and $\tau = 1$ (red) surfaces. The reference disk relaxes rapidly to a smooth hydrostatic configuration; the bulk of the realistic disk does so as well, although differences persist in the slowly-cooling disk atmosphere.

where ρ_{dg} is the bulk density of each dust grain and $v_{\text{th}} = \sqrt{8\pi k_B T_g / \mu m_H}$ is the gas thermal velocity. A quantity in angle brackets $\langle g(a_{\text{dg}}) \rangle$ represents the integral of that quantity over the (normalized) grain size distribution $n(a)$:

$$\langle g(a_{\text{dg}}) \rangle = \int_{a_{\text{min}}}^{a_{\text{max}}} g(a') n(a') da' \quad (29)$$

For our three-temperature tests of the SSI, we use the setup dg3t100 from Melon Fuksman & Klahr (2022), generated with the aforementioned iterative procedure, as the basis for our initial conditions. We employ a reduced speed of light $\hat{c} = 10^{-3} c$; our tests at $\hat{c}' = 5\hat{c} = 5 \times 10^{-3} c$ (not shown) yield converged results. The gas follows an ideal equation of state—with an adiabatic index $\gamma = 1.41$ and a mean molecular weight $\mu = 2.3$. We assume a total dust fraction of 1%, of which 10% by mass

($f_d = 10^{-3}$) are taken to be small grains relevant to the gas's thermal evolution. These grains are taken to consist of 62.5% silicate and 37.5% graphite, with a bulk density $\rho_{\text{gr}} = 2.5 \text{ g cm}^{-3}$ and a specific heat capacity $c_d = 0.7 \text{ J g}^{-1} \text{ K}^{-1}$; their sizes follow a classical MRN (Mathis et al. 1977) distribution, $n(a) \propto a^{-3.5}$, with $a_{\text{min}} = 5 \text{ nm}$ and $a_{\text{max}} = 250 \text{ nm}$.²

From these grain properties, we compute a temperature-dependent, frequency-integrated dust opacity $\kappa_D(T_d)$, based on the tabulated frequency-dependent figures by Krieger & Wolf (2020, 2022) as well as t_s . We additionally bracket the dust

² With the MRN distribution, $\langle a_{\text{dg}}^3 \rangle / \langle a_{\text{dg}}^2 \rangle = \sqrt{a_{\text{min}} a_{\text{max}}} = 35.4 \text{ nm}$, and dust fraction $f_d \propto \sqrt{a_{\text{max}} / a_{\text{min}}} - 1$. With these relations, it can be shown that the gas cooling time t_c (equation 5) converges to a fixed limiting value as long as $a_{\text{max}} \gg a_{\text{min}}$. Physically, this means that collisional energy exchange is dominated by the smallest grains.

stopping time to lie within $[10^{-10}/2\pi, 10^1/2\pi]$ years, and take $T_g \rightarrow \max(T_g, 10 \text{ K})$ for the purpose of computing v_{th} . We assume a classical T Tauri star with $M_* = 1M_\odot$, $R_* = 2.0865R_\odot$, and $T_* = 4000 \text{ K}$, to compute the dust irradiation source term S_d as well as the gravitational potential

$$\Phi_* = -\frac{GM_*}{r_*} \quad (30)$$

where $r_* \equiv \|\mathbf{x} - \mathbf{x}\|$ is the distance between the star and a given point in the domain. We plot the resulting initial condition, as well as relevant contours for radial optical depth τ_r and gas cooling parameter $\beta \equiv t_c \Omega = (2/3)(\gamma-1)^{-1} f_d^{-1} t_s \Omega$, in the upper panel of Figure 3. We emphasize that our β -cooling parameter reflects only gas-grain collisions; because we self-consistently model radiative transfer, we do not incorporate assumptions about time or length scales for radiative diffusion or optically thin cooling, as in some previous work (e.g., Bae et al. 2021).

We run our SSI simulation in 2D axisymmetric polar coordinates, with radial limits at $r = [0.4, 100]$ au and polar limits at $\theta = \pi/2 + [-0.23, 0.23]$. This domain is spanned by $\{N_r, N_\theta\} = \{512, 170\}$ grid cells, logarithmically spaced in the radial direction and uniformly spaced in polar angle. At the boundaries, all fields are set equal to those in `dg3t0_1`, the fiducial smooth hydrostatic setup in Melon Fuksman & Klahr (2022). We also include a damping zone in the region $\{r < r_{\text{damp.in}}\} \cup \{p < 0\}$, where $r_{\text{damp.in}} = 0.5 \text{ au}$ and $p \equiv -|\theta - \pi/2| + 0.12 + 0.13(r/\text{au})$. In this zone, we enforce $T_d = T_g$, while relaxing ρ and v to their smooth hydrostatic values on a timescale

$$t_{\text{damp}} = 0.1\Omega(r)^{-1} \cos^2[\pi/2(1 + p/p_+)] \quad (31a)$$

in the region where $s < 0$, and

$$t_{\text{damp}} = 0.1\Omega(r)^{-1} \cos^{-2}\left[\pi/2\left(\frac{r - r_{\text{in}}}{r_{\text{damp.in}} - r_{\text{in}}}\right)\right] \quad (31b)$$

elsewhere in the damping zone; we have tested alternative damping prescriptions and found no substantive change to our results. For comparison with the two-temperature regime, we also run a simulation with a fixed global stopping time $t_s = (2\pi)^{-1} \times 10^{-10} \text{ y}$, but otherwise identical.

In Figure 4 we plot T_d and T_g from our realistic three-temperature simulation, as well as the matter temperature T_{ref} in the two-temperature reference simulation, at $t = \{0, 1, 10, 100\} \text{ y}$. In the reference simulation, the initial scale-height perturbations at the $\tau_r = 1$ surface dissipate rapidly, and are almost completely absent by $t = 10 \text{ y}$, reproducing the results of the equivalent two-temperature runs in Melon Fuksman & Klahr (2022). Our three-temperature realistic simulation, in which $\beta \approx 1$ at the $\tau_r = 1$ surface, shows a similar evolution, as T_g still evolves too fast to achieve the smooth, columnar hydrostatic adaptation obtained in 1+1D and iterative approaches that reproduce the SSI. To better understand this temperature evolution, we plot in Figure 5 the time evolution of T_d , T_g , and T_{ref} —normalized by the final, relaxed reference temperature T_{relax} —in a fiducial disk column at $r = 2 \text{ au}$.

By $t = 10^2 \text{ y}$, the temperature profile within the $\tau_r = 1$ surface of the realistic simulation has largely reached the same smooth equilibrium as in the reference. The slow-cooling disk atmosphere in the realistic case—heated by waves emitted by the disk’s initial relaxation and reflecting off the boundaries—is too low in density and optical depth to substantively alter this picture. It remains an open question to what extent three-temperature methods can sustain the SSI. In this regard, our numerical experiments with a dust-gas coupling time artificially increased by 100× (described in Appendix B) show some promise,

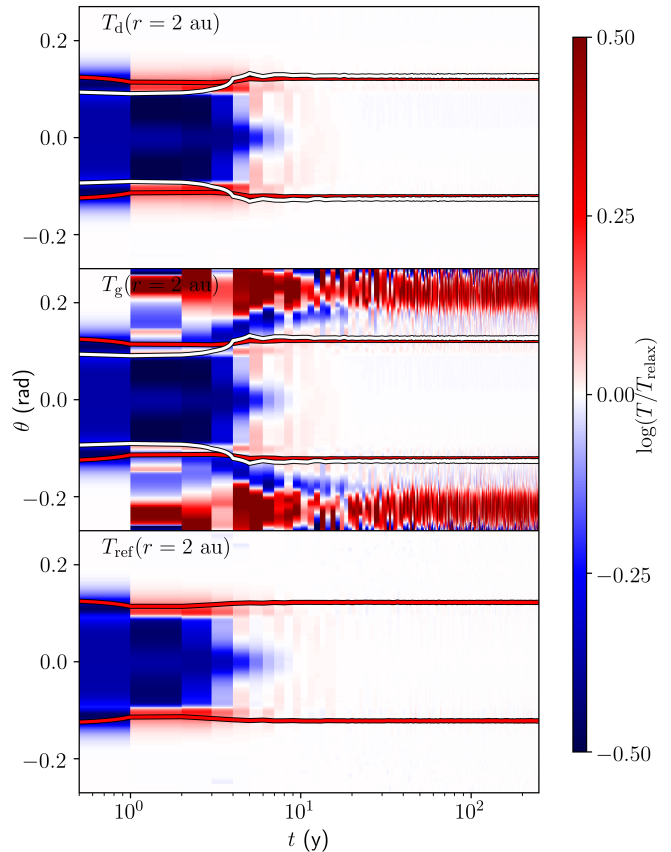


Fig. 5. Time evolution of T_d (top), T_g (center), and T_{ref} (bottom) in a disk column at the fiducial $r = 2 \text{ au}$, as compared to the final, relaxed state of T_{ref} . As in Figure 4, we plot the $\tau_r = 1$ optical surface in red and the $\beta = 1$ cooling surface in white. T_{ref} , as well as T_d and T_g , rapidly relax to a smooth equilibrium disk inside the $\beta = 1$ surface. Sound waves in the upper atmosphere—excited by the initial relaxation of the disk—are visible in T_g due to the slow cooling rate at high altitude.

allowing SSI waves to survive and propagate inward for roughly $\sim 10^2 \text{ y}$ before decaying.

3.4. 3D test: planet-driven spirals

In recent years, high-resolution observations in NIR (e.g., Benisty et al. 2015; Wagner et al. 2019; Xie et al. 2021) and in various molecular lines (e.g., Teague et al. 2019; Wölfer et al. 2021) have revealed spiral structures in circumstellar disks. It is hypothesized that some fraction of these are driven by embedded, planetary-mass companions (Goldreich & Tremaine 1978, 1979, 1980; Goodman & Rafikov 2001).

Early simulations of these spirals (e.g., Kley 1999) often used two-dimensional, vertically averaged setups, with a locally isothermal equation of state. Subsequent advances in computational power made it feasible to run disk-planet interaction simulations in full 3D (e.g., Fung & Dong 2015; Dong et al. 2016), relax the assumption of local isothermality (Zhu et al. 2015), and implement realistic vertical temperature structures (Juhász & Rosotti 2018)—which, in turn, enabled meaningful compar-

isons of simulated spirals to observations in dust (Dong & Fung 2017) and gas (Muley et al. 2021). More recently, Bae et al. (2021) used a parametrized cooling prescription to include the effects of matter-radiation interaction and gas-grain collisions. In what follows, we build on these previous works by modeling spirals with self-consistent, three-temperature radiation hydrodynamics.

For this test, we use the relaxed hydrostatic setup `dg3t0.1` from Melon Fuksman & Klahr (2022) as a starting point. The dust properties, stellar parameters, and cooling prescription are the same as in section 3.3, and we plot our initial condition, as well as the resulting contours for β and τ_r , in the lower panel of Figure 3. For this test, we use a $\hat{c} = 10^{-4}c$. Our simulation is run in 3D spherical coordinates, with radial boundaries at $r = [8, 100]$ au, polar boundaries at $\theta = \pi/2 + [-0.27, 0.27]$, and azimuthal boundaries at $\phi = [0, 2\pi]$; this simulation box is covered by $\{N_r, N_\theta, N_\phi\} = \{234, 54, 583\}$ cells, logarithmic in radius and uniform in azimuthal and polar angle. All fields are fixed to their initial values at the radial and azimuthal boundaries, and periodic at the azimuthal boundary.

In addition to the star and its gravitational potential Φ_* , our simulation includes a $q \equiv M_p/M_* = 10^{-3}$ planet ($M_p \approx 1.05M_J$), fixed on a circular Keplerian orbit with semimajor axis $a_p = 20$ au; given our temperature profile, this is $q_{\text{th}} = 5.5$ times the thermal mass. The planetary potential is given, following Klahr & Kley (2006), by

$$\Phi_p = -\frac{GM_p}{r_p} \begin{cases} 1 & \text{if } r_p \geq r_s \\ ([r_p/r_s]^4 - 2[r_p/r_s]^3 + 2[r_p/r_s]) & \text{if } r_p < r_s \end{cases} \quad (32)$$

where $r_p \equiv \|\mathbf{x} - \mathbf{x}_p\|$ is the distance between the planet and a point in our domain, and r_s is the smoothing length, implemented to avoid a singularity in the potential. In our simulations, we set $r_s = r_H/2$.

To avoid unphysically shocking the disk at early times, we introduce this companion at $t_i = 1$ y and grow it from zero to its final mass over the following $t_{\text{grow}} = 10$ y. We solve our equations in the planet's co-rotating frame, fixing its azimuthal coordinate as $\phi_p = \pi/4$. In this frame, the pattern speed of the spiral, and consequently of the non-axisymmetric radiation field, is zero; deviations would be of order $c_s \approx 10^{-6}c \approx 10^{-2}\hat{c}$. Numerical tests at $\hat{c}' = 2 \times 10^{-5} = \hat{c}/5$, not shown here, yield a well-converged spiral amplitude. To prevent the growth of large-scale disk instabilities such as the Rossby wave instability (RWI Lovelace & Romanova 2014), we include a kinematic viscosity $\nu = \alpha c_s^2 \Omega^{-1}$, where $\alpha = 0.001$ is the Shakura & Sunyaev (1973) viscosity parameter. As in section 3.3, we run a three-temperature realistic simulation, as well as an otherwise-identical reference simulation with $t_s = (2\pi)^{-1} \times 10^{-10}$ y.

To keep focus on the spirals, we analyze the snapshot at $t_{\text{cut}} = 500$ y, before our super-thermal planet has had the chance to carve a gap in the disk. In Figure 6, we present gas densities in our three-temperature realistic (ρ_{gas}) and two-temperature reference (ρ_{ref}) simulations, taken at $r = 30$ au and $\theta = \{0, 0.15, 0.2\}$. At $\theta = 0$, the primary and secondary Lindblad spirals are visible in both ρ_{gas} and ρ_{ref} , and agree to within several percent. This is expected, because the three-temperature midplane $\beta \lesssim 10^{-2}$ and reference simulation global $\beta \lesssim 10^{-11}$ are both much shorter than the spiral-crossing timescale, $\beta_{\text{spiral}} \approx (h/r)|1 - \Omega_p/\Omega_{30}|^{-1}$ (Sturm et al. 2020) where Ω_{30} is the Keplerian frequency at 30 au. In the upper disk, the realistic $\beta \approx 1$ exceeds β_{spiral} , while the reference β remains unchanged. Due to this difference in thermal physics, the density structures become discrepant at the $\sim 20\%$

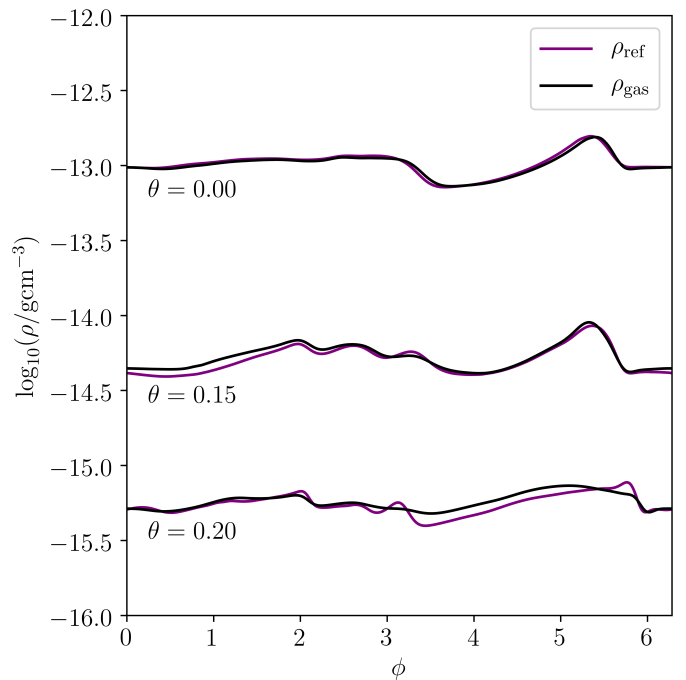


Fig. 6. Density values for our three-temperature realistic (ρ_{gas}) and reference (ρ_{ref}) simulations, taken at the indicated θ values at a fixed $r = 30$ au. Densities largely agree to within a few percent between both models, but the discrepancy rises to $\sim 20\%$ at the $\tau_r = 1$ surface, causing a mild impact on the temperature structure below.

level, with Lindblad spirals being more sharply defined in ρ_{ref} than in ρ_{gas} .

In Figure 7, we plot temperatures at the same cuts studied in Figure 6. In the midplane of our three-temperature simulation, strong dust-gas coupling ensures that T_d and T_g are equal. At $\theta = 0.15$, dust-gas coupling is somewhat weaker, with a $\beta \approx 10^{-1} \approx \beta_{\text{spiral}}$, and differences between T_d and T_g are visible throughout the azimuthal extent of our cut. High in the disk atmosphere, at $\theta = 0.2$, the normalized cooling time is $\beta \approx 1$, much longer than the spiral-crossing timescale for gas. Here, we observe a spiral feature in T_g with an amplitude $\sim 10\%$ —comparable to that found the $\beta = 1$, $M_p = 400M_{\oplus}$ spiral simulation in Muley et al. (2021)—which is not visible in T_d or T_{ref} .

At $\theta = 0$, we observe a slight temperature dip centered at $\phi = \phi_p = \pi/4$, while at $\theta = 0.15$ and $\theta = 0.2$, we find a temperature bump at the same azimuthal position. This is ultimately caused by the gravitational influence of the planet, which lowers the $\tau_r = 1$ surface overhead and thus changes the illumination of material in the radial band $\phi \approx \phi_p$, $r \gtrsim r_p$. Such a feature was also observed in the Monte Carlo radiative transfer post-processing of Muley et al. (2021)'s hydrodynamical simulations.

To provide a more visual understanding of these results, we present 2D polar cuts of T_d , T_g , and T_{ref} , at $\theta = 0.0$ and $\theta = 0.2$, in Figure 8. We find, as in our 1D quantitative plots, that the morphology of T_{ref} largely agrees with that of T_d , despite substantial differences in β between and within each simulation, while T_g and T_d only agree with one another when $\beta < \beta_{\text{spiral}}$. We interpret this to imply that T_d is set by the very short timescales for dust collisional energy exchange $t_{\text{c,dust}} = r_{\text{gd}}^{-1} t_c$ (following equation 6) and for radiative cooling, either vertically or in-plane (Miranda & Rafikov 2020a; Ziampras et al. 2020). How T_g , in turn, reacts to the dust depends on the much longer local gas cooling time $t_c = \beta/\Omega$ —a result that could affect the observational signatures

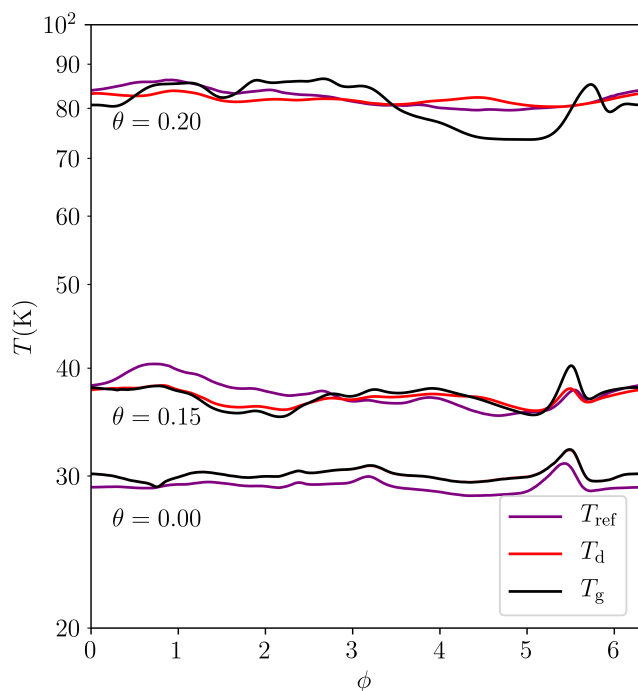


Fig. 7. Temperatures in our three-temperature realistic ($T_{\text{gas}}, T_{\text{dust}}$) and reference (T_{ref}) simulations, taken at the same cuts as in Figure 6. In the midplane, where coupling times are short, $T_{\text{gas}} = T_{\text{dust}}$, but in the disk atmosphere, where coupling is weaker, there is a noticeable ($\sim 10\%$) discrepancy between the two: T_{dust} reflects the stellar irradiation field, while T_{gas} is driven by the PdV work done by the planetary spiral.

disk-planet interaction produces in gas and dust. We note, in addition, a slight discrepancy between the background T_{dust} and T_{ref} , with the latter being systematically lower throughout the disk; this is because spirals are more vertically extended in the two-temperature limit, and so cast stronger shadows throughout the disk. We intend to investigate these issues further in a future study.

4. Conclusion

We have developed an implicit-explicit (IMEX) numerical scheme for the PLUTO hydrodynamics code to self-consistently model energy exchange between gas, dust, and radiation. The implicit substep, consisting of nonrelativistic matter-radiation interaction source terms, is solved iteratively with a multidimensional Newton-Raphson method, whereas the explicit substep, consisting of radiation transport and relativistic interaction source terms, is solved using a Godunov scheme, following Melon Fuksman & Mignone (2019). Because this explicit part is Courant-limited, we use the reduced speed of light approximation, as implemented by Melon Fuksman et al. (2021), to improve computational efficiency. This gives physically reasonable results, so long as the reduced speed of light \hat{c} is much larger than all other relevant velocities in the problem.

In our 0D matter-radiation coupling test, we demonstrate the ability of our scheme to reproduce the “two-temperature” regime of traditional radiation hydrodynamics, where dust and gas are well-coupled. For the 1D Ensmann (1994) shock tube test, we relax this assumption, and investigate the behavior of gas, dust, and radiation temperatures in different coupling regimes. Our subsequent tests illustrate the applicability of three-temperature radiation hydrodynamics to active problems in circumstellar disk re-

search, including realistic opacities and dust-gas coupling times computed from local temperature and density. Our 2D test shows that the self-shadowing instability—which arises in 1+1D time-dependent models with parametrized disk scale height, as well as 2D iterative techniques that alternate the calculation of radiative and hydrostatic equilibrium—decays rapidly in the two-temperature limit, as well as with realistic three-temperature coupling times, in line with previous expectations (Melon Fuksman & Klahr 2022). However, an increased cooling time (Appendix B) allows dust temperatures in most of the disk column to rapidly adapt to stellar irradiation before the gas can react—which better satisfies the key assumptions of the aforementioned iterative and 1D-hydrostatic methods, and so allows SSI-type scale-height perturbations to survive for somewhat longer before decaying. In our 3D spiral simulations, dust temperatures are remarkably consistent between the two- and three-temperature regimes, but gas temperatures disagree in the upper atmosphere—a result with implications for observations of spirals in gas tracers such as ^{12}CO . Future potential applications of our three-temperature scheme include studies of circumplanetary disk accretion shocks, planetary gap opening, photoevaporation, and hydrodynamic/MHD instabilities such as the vertical shear instability, among many others.

Our scheme makes the simplifications that dust and gas move at the same velocity, and that dust inertia is negligible ($\text{St} \equiv t_s \Omega \ll 1$, $f_d \ll 1$). While these are reasonable assumptions for the sub- μm grains that supply most of a disk’s total opacity and set its overall thermal structure, they are invalid for the millimeter grains that concentrate at pressure maxima and produce much of its continuum emission. Including such grains would require accounting for multispecies momentum transfer including back-reaction from the gas (using schemes such as those detailed in e.g., Benítez-Llambay et al. 2019; Huang & Bai 2022) and thermal coupling. While such a method would be immensely helpful in interpreting continuum observations of gaps, rings, and spirals, it would be computationally demanding and require extensive testing beyond the scope of this work.

Acknowledgements. We thank Remo Burn, Cornelis Dullemond, Mario Flock, Thomas Henning, Carolin Kimmig, Giancarlo Mattia, Thomas Rometsch, and Prakruti Sudarshan for useful discussions. We are also grateful to the anonymous referee, whose report helped improve the quality of this paper. All numerical simulations were performed on the Cobra cluster of the Max Planck Society and the Vera Cluster of the Max Planck Institut für Astronomie, both hosted by the Max Planck Computing and Data Facility (MPCDF) in Garching bei München. The research of J.D.M.F. and H.K. is supported by the German Science Foundation (DFG) under the priority program SPP 1992: “Exoplanet Diversity” under contract KL 1469/16-1/2.

References

- Bae, J., Teague, R., & Zhu, Z. 2021, *ApJ*, 912, 56
- Bate, M. R. & Keto, E. R. 2015, *MNRAS*, 449, 2643
- Benisty, M., Juhasz, A., Boccaletti, A., et al. 2015, *A&A*, 578, L6
- Benítez-Llambay, P., Krapp, L., & Pessah, M. E. 2019, *ApJS*, 241, 25
- Binkert, F., Szulágyi, J., & Birnstiel, T. 2023, *MNRAS*
- Bitsch, B., Crida, A., Morbidelli, A., Kley, W., & Dobbs-Dixon, I. 2013, *A&A*, 549, A124
- Bruderer, S. 2013, *A&A*, 559, A46
- Bruderer, S., van Dishoeck, E. F., Doty, S. D., & Herczeg, G. J. 2012, *A&A*, 541, A91
- Burke, J. R. & Hollenbach, D. J. 1983, *ApJ*, 265, 223
- Calahan, J. K., Bergin, E. A., Zhang, K., et al. 2021, *ApJS*, 257, 17
- Chiang, E. I. & Goldreich, P. 1997, *ApJ*, 490, 368
- D’Alessio, P., Cantó, J., Hartmann, L., Calvet, N., & Lizano, S. 1999, *ApJ*, 511, 896
- Dong, R. & Fung, J. 2017, *ApJ*, 835, 38
- Dong, R., Fung, J., & Chiang, E. 2016, *ApJ*, 826, 75
- Dullemond, C. P. 2000, *A&A*, 361, L17

- Dullemond, C. P., Hollenbach, D., Kamp, I., & D'Alessio, P. 2007, in *Protostars and Planets V*, ed. B. Reipurth, D. Jewitt, & K. Keil, 555
- Dullemond, C. P., Juhasz, A., Pohl, A., et al. 2012, RADMC-3D: A multi-purpose radiative transfer tool, *Astrophysics Source Code Library*, record ascl:1202.015
- Ensmann, L. 1994, *ApJ*, 424, 275
- Flock, M., Fromang, S., González, M., & Commerçon, B. 2013, *A&A*, 560, A43
- Flock, M., Turner, N. J., Nelson, R. P., et al. 2020, *ApJ*, 897, 155
- Fung, J. & Dong, R. 2015, *ApJ*, 815, L21
- Fung, J., Zhu, Z., & Chiang, E. 2019, *ApJ*, 887, 152
- Gnedin, N. Y. & Abel, T. 2001, *New A*, 6, 437
- Goldreich, P. & Tremaine, S. 1978, *ApJ*, 222, 850
- Goldreich, P. & Tremaine, S. 1979, *ApJ*, 233, 857
- Goldreich, P. & Tremaine, S. 1980, *ApJ*, 241, 425
- Goodman, J. & Rafikov, R. R. 2001, *ApJ*, 552, 793
- Hu, X., Li, Z.-Y., Wang, L., Zhu, Z., & Bae, J. 2023, arXiv e-prints, arXiv:2304.05972
- Huang, P. & Bai, X.-N. 2022, *ApJS*, 262, 11
- Huang, S. & Yu, C. 2022, *MNRAS*, 514, 1733
- Hubeny, I. 1990, *ApJ*, 351, 632
- Juhász, A. & Rosotti, G. P. 2018, *MNRAS*, 474, L32
- Keppler, M., Benisty, M., Müller, A., et al. 2018, *A&A*, 617, A44
- Klahr, H. & Kley, W. 2006, *A&A*, 445, 747
- Kley, W. 1999, *MNRAS*, 303, 696
- Kley, W., Bitsch, B., & Klahr, H. 2009, *A&A*, 506, 971
- Krieger, A. & Wolf, S. 2020, *A&A*, 635, A148
- Krieger, A. & Wolf, S. 2022, *A&A*, 662, A99
- Levermore, C. D. 1984, *J. Quant. Spectr. Rad. Transf.*, 31, 149
- Levermore, C. D. & Pomraning, G. C. 1981, *ApJ*, 248, 321
- Lovelace, R. V. E. & Romanova, M. M. 2014, *Fluid Dynamics Research*, 46, 041401
- Malygin, M. G., Klahr, H., Semenov, D., Henning, T., & Dullemond, C. P. 2017, *A&A*, 605, A30
- Manger, N., Pfeil, T., & Klahr, H. 2021, *MNRAS*, 508, 5402
- Mathis, J. S., Rimpl, W., & Nordsieck, K. H. 1977, *ApJ*, 217, 425
- Melon Fuksman, J. D., Flock, M., & Klahr, H. 2023, *A&A*, submitted
- Melon Fuksman, J. D. & Klahr, H. 2022, *ApJ*, 936, 16
- Melon Fuksman, J. D., Klahr, H., Flock, M., & Mignone, A. 2021, *ApJ*, 906, 78
- Melon Fuksman, J. D. & Mignone, A. 2019, *ApJS*, 242, 20
- Mignone, A., Bodo, G., Massaglia, S., et al. 2007, *ApJS*, 170, 228
- Miranda, R. & Rafikov, R. R. 2019, *The Astrophysical Journal Letters*, 878, L9
- Miranda, R. & Rafikov, R. R. 2020a, *ApJ*, 904, 121
- Miranda, R. & Rafikov, R. R. 2020b, *ApJ*, 892, 65
- Muley, D., Dong, R., & Fung, J. 2021, *AJ*, 162, 129
- Pareschi, L. & Russo, G. 2005, *Journal of Scientific Computing*, 25, 129
- Pavlyuchenkov, Y. N. & Zhilkin, A. G. 2013, *Astronomy Reports*, 57, 641
- Pavlyuchenkov, Y. N., Zhilkin, A. G., Vorobyov, E. I., & Fateeva, A. M. 2015, *Astronomy Reports*, 59, 133
- Pierens, A. & Lin, M.-K. 2018, *MNRAS*, 479, 4878
- Pinte, C., Teague, R., Flaherty, K., et al. 2022, arXiv e-prints, arXiv:2203.09528
- Ren, B., Dong, R., Esposito, T. M., et al. 2018, *ApJ*, 857, L9
- Shakura, N. I. & Sunyaev, R. A. 1973, *A&A*, 24, 337
- Skinner, M. A. & Ostriker, E. C. 2013, *ApJS*, 206, 21
- Speedie, J., Booth, R. A., & Dong, R. 2022, *ApJ*, 930, 40
- Sturm, J. A., Rosotti, G. P., & Dominik, C. 2020, *A&A*, 643, A92
- Tarczay-Nehéz, D., Regály, Z., & Vorobyov, E. 2020, *MNRAS*, 493, 3014
- Teague, R., Bae, J., Huang, J., & Bergin, E. A. 2019, *ApJ*, 884, L56
- Ueda, T., Flock, M., & Birnstiel, T. 2021, *ApJ*, 914, L38
- Ueda, T., Flock, M., & Okuzumi, S. 2019, *ApJ*, 871, 10
- Vorobyov, E. I., Matsukoba, R., Omukai, K., & Guedel, M. 2020, *A&A*, 638, A102
- Wagner, K., Stone, J. M., Spalding, E., et al. 2019, *ApJ*, 882, 20
- Wang, L., Bai, X.-N., & Goodman, J. 2019, *ApJ*, 874, 90
- Wang, L. & Goodman, J. 2017, *ApJ*, 847, 11
- Watanabe, S.-i. & Lin, D. N. C. 2008, *ApJ*, 672, 1183
- Whitney, B. A., Robitaille, T. P., Bjorkman, J. E., et al. 2013, *ApJS*, 207, 30
- Woitke, P., Kamp, I., & Thi, W. F. 2009, *A&A*, 501, 383
- Wölfer, L., Facchini, S., Kurtovic, N. T., et al. 2021, *A&A*, 648, A19
- Wu, Y. & Lithwick, Y. 2021, *ApJ*, 923, 123
- Xie, C., Ren, B., Dong, R., et al. 2021, *ApJ*, 906, L9
- Yamaleev, N. K. & Carpenter, M. H. 2009, *Journal of Computational Physics*, 228, 3025
- Zhang, S. & Zhu, Z. 2020, *MNRAS*, 493, 2287
- Zhu, Z., Dong, R., Stone, J. M., & Rafikov, R. R. 2015, *ApJ*, 813, 88
- Ziampras, A., Kley, W., & Dullemond, C. P. 2020, *A&A*, 637, A50

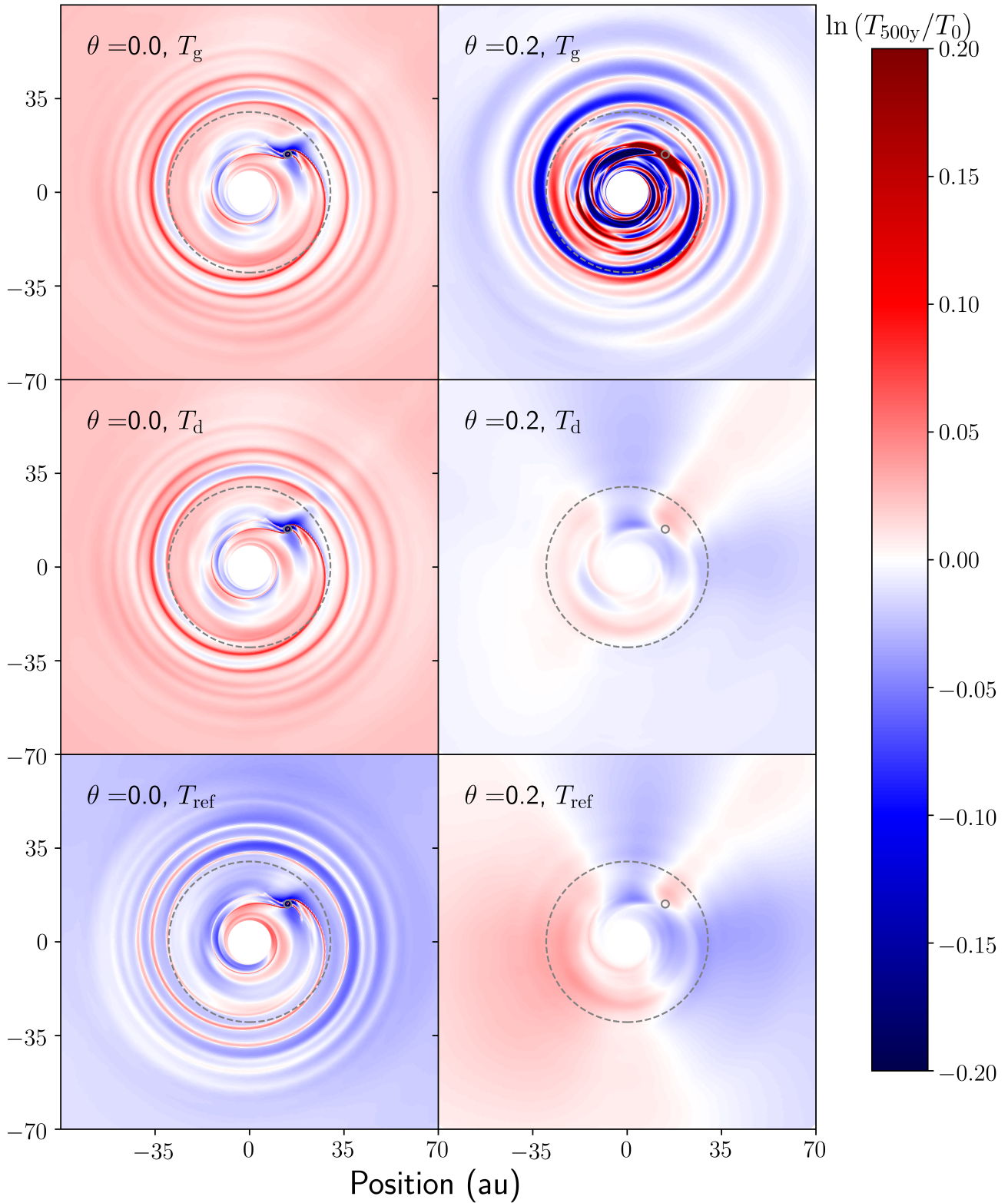


Fig. 8. Relative difference between the temperature at $t_{\text{cut}} = 500$ y and the initial profile, in polar cuts at $\theta = 0.0$ and $\theta = 0.2$. The morphology of T_d and T_g agree in the midplane, but diverge at higher altitude, while the morphology of T_d and T_{ref} agree everywhere. In each panel, we indicate the Hill sphere of the planet with a small *solid grey* circle, and our cuts in figures 6 and 7 with a large *dotted grey* circle.

Appendix A: Newton-Raphson iterations

We rearrange eqs. (18a) and (18b) as a vector of quantities

$\mathbf{P}(\xi_{\text{sub}}^{i+1}) \equiv (P_d, P_g)^\top$, where $\xi_{\text{sub}}^{i+1} \equiv (\xi_d^{i+1}, \xi_g^{i+1})$.

$$P_d = \xi_d^i - \xi_d^{i+1} - t_c^{-1} \left[r_{gd} \xi_d^{i+1} - \xi_g^{i+1} \right] \delta t - c \rho \kappa_d^{i+1} f_d \left[a_r (T_d^{i+1})^4 - \xi_r^{i+1} \right] \delta t + S_d \delta t \quad (\text{A.1})$$

$$P_g = \xi_g^i - \xi_g^{i+1} + t_c^{-1} \left[r_{gd} \xi_d^{i+1} - \xi_g^{i+1} \right] \delta t - c \rho \kappa_g^{i+1} \left[a_r (T_g^{i+1})^4 - \xi_r^{i+1} \right] \delta t + S_g \delta t \quad (\text{A.2})$$

where

$$\xi_r^{i+1} = \xi_r^i - \frac{\hat{c}}{c} \left[(\xi_d^{i+1} - \xi_d^i) + (\xi_g^{i+1} - \xi_g^i) \right] \quad (\text{A.3})$$

Using Newton's method, we attempt to find a vector $\xi^{i+1,*}$, such that $\mathbf{P}(\xi^{i+1,*}) = \mathbf{0}$ to within some small tolerance α . The relevant Jacobian matrix $\mathbf{J}(\xi^{i+1}) \equiv \partial \mathbf{P} / \partial \xi^{i+1}$ is:

$$\mathbf{J}(\xi_{\text{sub}}^{i+1}) = \begin{bmatrix} \partial P_d / \partial \xi_d^{i+1} & \partial P_d / \partial \xi_g^{i+1} \\ \partial P_g / \partial \xi_d^{i+1} & \partial P_g / \partial \xi_g^{i+1} \end{bmatrix} \quad (\text{A.4})$$

where

$$\partial P_d / \partial \xi_d^{i+1} = -(1 + r_{gd} \delta t / t_c) - c \rho \kappa_d^{i+1} f_d \delta t \left[4 a_r (T_d^{i+1})^3 / \rho f_d c_d + \hat{c} / c \right] \quad (\text{A.5})$$

$$\partial P_d / \partial \xi_g^{i+1} = +\delta t / t_c - \hat{c} \rho \kappa_d^{i+1} f_d \delta t \quad (\text{A.6})$$

$$\partial P_g / \partial \xi_d^{i+1} = +r_{gd} \delta t / t_c - \hat{c} \rho \kappa_g^{i+1} \delta t \quad (\text{A.7})$$

$$\partial P_g / \partial \xi_g^{i+1} = -(1 + \delta t / t_c) - c \rho \kappa_g^{i+1} \delta t \left[4 a_r (T_g^{i+1})^3 / \rho c_g + \hat{c} / c \right] \quad (\text{A.8})$$

We omit terms dependent on the derivatives of opacity and cooling time, although (these being, in general, functions of temperature) we update them with each iteration of Newton's method. The update goes as:

$$\mathbf{J}(\xi_n^{i+1}) \left[\xi_{n+1}^{i+1} - \xi_n^{i+1} \right] = -\mathbf{P}_n \quad (\text{A.9})$$

where n is an iteration index, in contrast to the timestep index i .

Appendix B: Self-shadowing instability with long coupling times

Our investigation in Section 3.3 found that, just as in the two-temperature case, our "realistic" three-temperature disk with self-consistently evaluated dust-gas coupling times cannot sustain the self-shadowing instability (SSI). This result, however, leaves open the question of whether there is any circumstance under which three-temperature dynamics could favor the survival of the SSI. To study this possibility, we ran a simulation with dust-gas coupling times 100× larger than those in the realistic run in Section 3.3. To facilitate comparison with our previous results, we hold all other simulation parameters—including, crucially, the dust opacity prescription and dust-to-gas ratio—fixed. Formally, solving for t_s in Equation 5, this would imply a

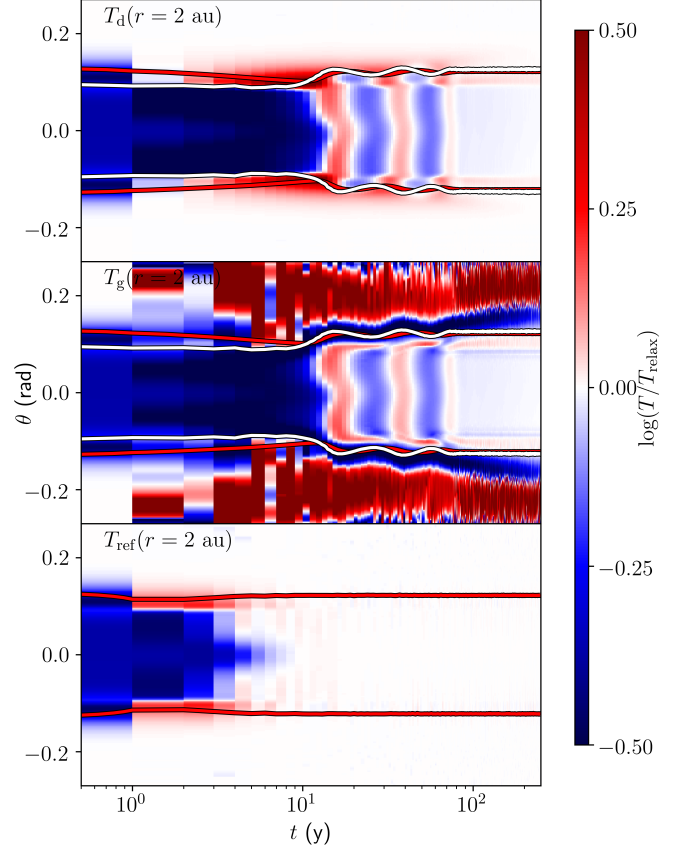


Fig. B.1. A plot similar to our Figure 5, but with T_d and T_g taken from our simulation with cooling times artificially raised by a factor of 100. There are clear vertical patterns in the dust and gas temperature profiles, corresponding to inward-traveling perturbations at the $\tau_r = 1$ surface characteristic of the SSI.

Stokes number $St \approx 0.06$ for grains at the $\tau_r = 1$ surface, which can be expected to experience vertical drift. However, we emphasize that this 100×-cooling setup is artificial, and is designed to approximate and long relaxation times that arise in disk upper atmospheres in detailed calculations of grain growth, settling, and depletion (see e.g., Bae et al. 2021, for one such scenario). The dust populations arising from these calculations are, by construction, in steady state, and do not experience net vertical drift.

In Figure B.1, we plot the time evolution of T_d , T_g , and T_{ref} —normalized by the final, relaxed reference temperature T_{relax} —in a fiducial disk column at $r = 2$ au. In the two-temperature reference simulation, the initialized self-shadowing perturbations rapidly decay (as already evident from Figure 4), but in the three-temperature 100× realistic simulation, they survive for some time, as evidenced by the vertical bands in T_d and T_g between $t = 10^1 - 10^2$ y.

At the leading edge of a self-shadowing scale-height perturbation, the flaring angle of the $\tau_r = 1$ is high and intercepts more direct stellar irradiation. Although T_d reflects this change immediately, the fact that $\beta \gg 1$ in this disk region means that the response of T_g —and the consequent vertical expansion of the gas column to seek hydrostatic equilibrium—is significantly slower.

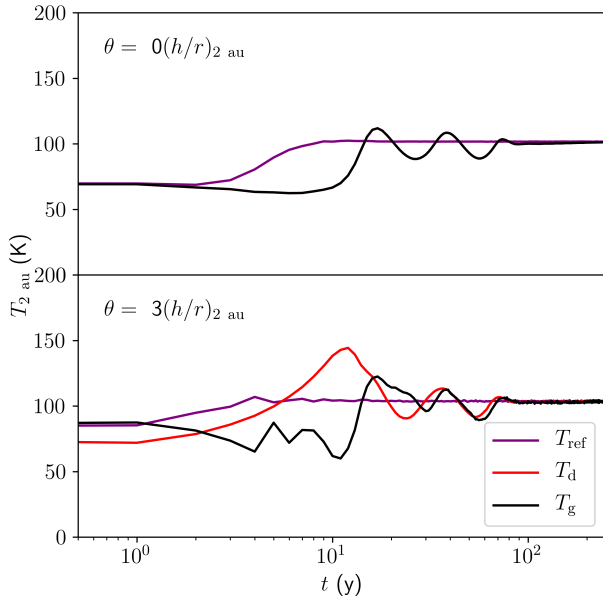


Fig. B.2. Quantitative time evolution of T_d and T_g from the $100\times$ -realistic simulation, and T_{ref} in the reference simulation, at $r = 2$ au, both in the midplane ($\theta = 0$, *above*) and 3 scale heights above it ($\theta \approx 0.088$, *below*). As qualitatively shown in Figure B.1, T_{ref} reaches a smooth equilibrium, whereas T_d and T_g exhibit damped oscillations due to the passage of self-shadowing waves. See text for more details.

As the gas column puffs up, it creates a new leading edge immediately to its interior; when this edge puffs up in turn, it blocks stellar irradiation from reaching the original column, causing it to cool and shrink. In this fashion, self-shadowing waves can propagate inward towards the star purely through vertical motions of the fluid elements. This mechanism would not operate when dust and gas are well-coupled; in that regime, both components would have a common temperature, and would respond to surface perturbations via layered radiative diffusion. The long timescale for this diffusion—given very roughly by Equation 27)—means that surface perturbations would decay before having an effect deep in the disk (Melon Fuksman & Klahr 2022).

For a more quantitative view, we present in Figure B.2 the time evolution of T_d , T_g , and T_{ref} at $r = 2$ au and $\theta = \pi/2 + \{0.0, 0.088\}$ (the latter θ corresponding to 3 scale heights above the midplane). At both altitudes, T_{ref} relaxes almost immediately to its hydrostatic equilibrium value, where it remains for the rest of the simulation. The evolution of T_d and T_g is more complex. High in the disk, the dust temperature rises interior to self-shadowing bumps, and drops exterior to them; with some delay due to gas cooling parameters $\beta \approx 1$, T_d relaxes toward T_g and the interior and exterior gas columns adapt to the new hydrostatic equilibrium. The net result, as mentioned earlier and in line with typical expectations for the SSI, is the apparent inward propagation of self-shadowing bumps. The changes these bumps make to the disk’s illumination profile impact the midplane temperature, albeit with some delay and attenuation due to radiative diffusion.

In Figure B.3, we present snapshots of the full long-coupling disk at selected times. Puffed-up disk columns heated above the background temperature—a hallmark signature of self-shadowing waves—are clearly visible here, and are captured in Figures B.1 and B.2 as they travel inward through $r = 2$ au. By

$t = 250$ y, however, the long-cooling disk has largely relaxed to the same smooth equilibrium as the reference disk. Differences persist in the very slowly-cooling disk atmosphere, as well as in the $r \lesssim 1$ au region in the immediate vicinity of our fixed inner radial boundary.

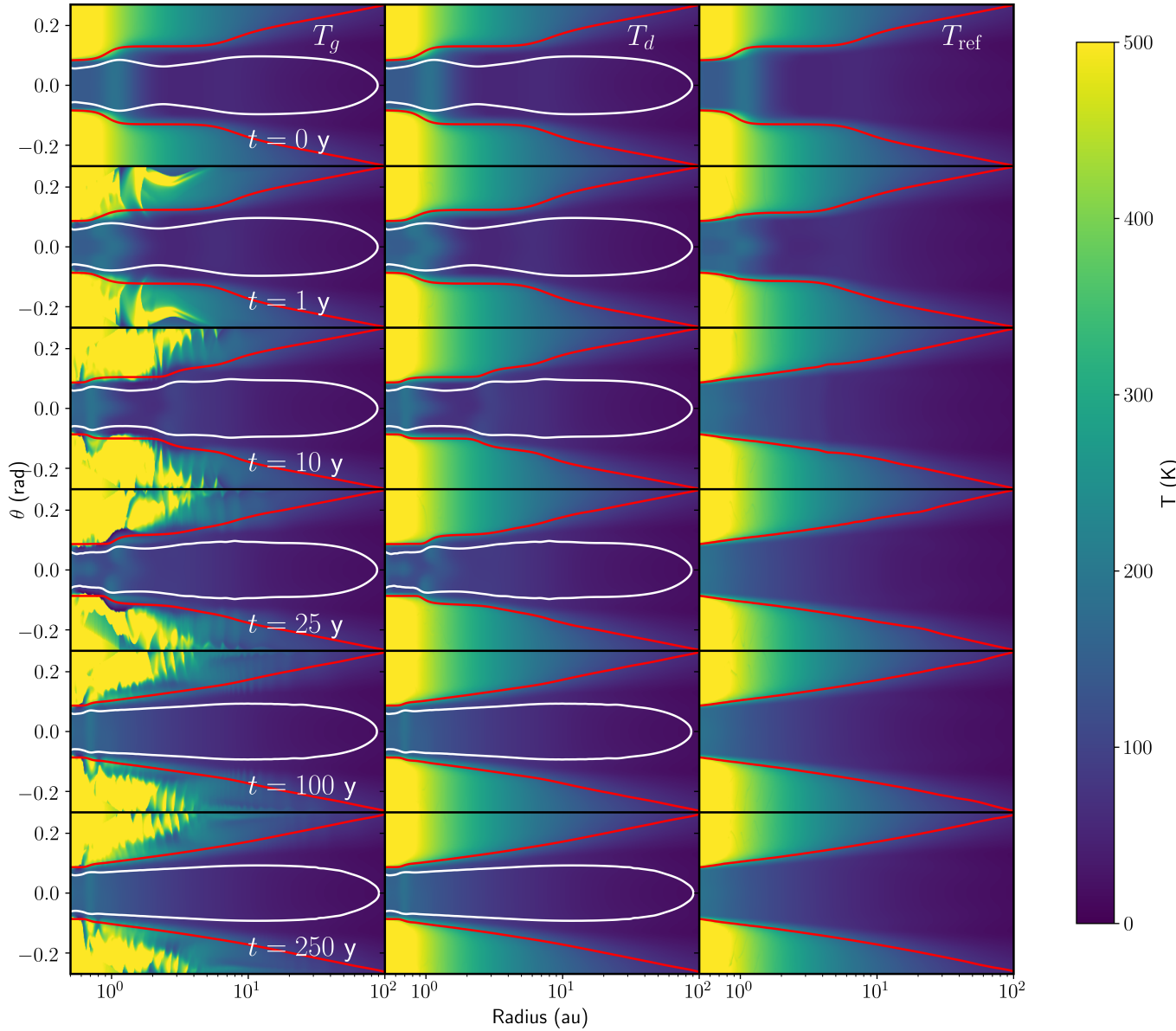


Fig. B.3. Evolution of the SSI with a dust-gas coupling time 100× longer than in the self-consistent setup presented in 3.3. An inward-propagating SSI bump is clearly visible. At $t = 250$ y, the disk has largely relaxed to the same configuration as in the reference simulation. Differences do persist, however, outside the $\beta = 1$ surface and near the inner boundary.